

OmniLens: Towards Universal Lens Aberration Correction via LensLib-to-Specific Domain Adaptation

Qi Jiang^{1,*} Yao Gao^{1,*} Shaohua Gao¹ Zhonghua Yi¹ Xiaolong Qian¹ Hao Shi^{1,2}
 Kailun Yang³ Lei Sun^{1,4,†} Kaiwei Wang^{1,†}
¹Zhejiang University ²Nanyang Technological University
³Hunan University ⁴INSAIT, Sofia University “St. Kliment Ohridski”

Abstract

Emerging universal Computational Aberration Correction (CAC) paradigms provide an inspiring solution to lightweight and high-quality imaging with a universal model trained on a lens library (LensLib) to address arbitrary lens aberrations blindly. However, the limited coverage of existing LensLibs leads to poor generalization of the trained models to unseen lenses, whose fine-tuning pipeline is also confined to the lens-descriptions-known case. In this work, we introduce OmniLens, a flexible solution to universal CAC via (i) establishing a convincing LensLib with comprehensive coverage for pre-training a robust base model, and (ii) adapting the model to any specific lens designs with unknown lens descriptions via fast LensLib-to-specific domain adaptation. To achieve these, an Evolution-based Automatic Optical Design (EAOD) pipeline is proposed to generate a rich variety of lens samples with realistic aberration behaviors. Then, we design an unsupervised regularization term for efficient domain adaptation on a few easily accessible real-captured images based on the statistical observation of dark channel priors in degradation induced by lens aberrations. Extensive experiments demonstrate that the LensLib generated by EAOD effectively develops a universal CAC model with strong generalization capabilities, which can also improve the non-blind lens-specific methods by 0.35~1.81dB in PSNR. Additionally, the proposed domain adaptation method significantly improves the base model, especially in severe aberration cases (at most 2.59dB in PSNR). The code and data will be available at <https://github.com/zju-jiangqi/OmniLens>.

1. Introduction

Computational Aberration Correction (CAC), equipped with a post-image-restoration method to deal with the degradation (*i.e.*, the optical degradation [5]) induced by

*Equal contribution.

†Correspondence: leo.sun@zju.edu.cn, wangkaiwei@zju.edu.cn.

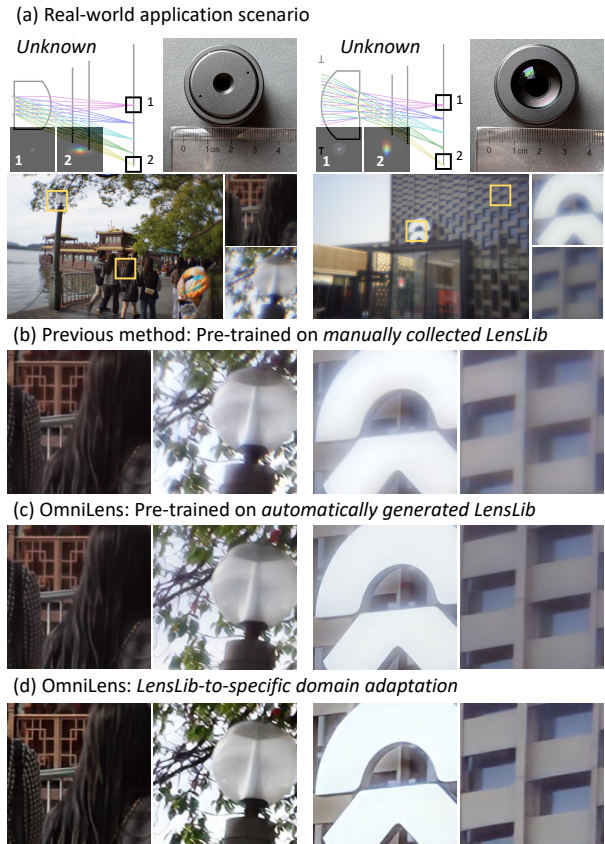


Figure 1. **OmniLens is a flexible solution to universal CAC.** In real-world cases of unknown lens descriptions for the applied low-end lenses, the pre-trained model with manually collected LensLib [31] delivers poor performance and can hardly be further fine-tuned. In contrast, the automatically generated LensLib in OmniLens develops a more robust model, where the LensLib-to-specific domain adaptation can further enhance the results.

residual optical aberrations of the target optical lens, is a fundamental and long-standing task [27, 42] in computational imaging. This technology is particularly highly demanded in mobile and wearable vision terminals for lightweight and high-quality photography [48, 62], where low-end lenses [13, 18] with simple structure and severe

optical degradation are applied, as shown in Fig. 1 (a). Recent advances in CAC have centered around Deep Learning (DL) based methods [4, 7, 36] equipped with a powerful image restoration network [3, 34, 59] being trained on the corresponding data pairs under lens-specific optical degradation [4, 5]. However, these methods have invariably been tailored to a specific lens, revealing limited generalization ability to other different lens designs. In this way, the complex and time-consuming pipeline of lens description calibration, imaging simulation, data preparation, and model training requires re-conduction for every new lens, limiting the applications of lens-specific CAC methods.

Consequently, developing a universal CAC model trained on datasets under a lens library (LensLib) to address arbitrary optical degradation has hit the forefront. Yet, existing solutions [14, 31] suffer two main limitations: (i) *the coverage of the manually collected LensLib is limited and inflexible for expanding*, leading to poor zero-shot CAC results when the target lens appears as a new, previously unseen sample, as shown in Fig. 1 (b); (ii) *the fine-tuning strategy [31] for model adaptation requires known or calibrated lens descriptions for data preparation*, which can hardly be achieved in real-world applications. Recently, the blooming development of Domain Adaptation (DA) [51, 53, 55] provides an effective pipeline to adapt the model trained on sufficient labeled data to unlabeled data with domain shift, which reveals potential in tuning the universal CAC model for a description-unknown lens, but has not been explored.

In this work, we build up a flexible universal CAC framework OmniLens, modeling the CAC as the problem of domain adaptation from a large LensLib to specific lenses. First and foremost, a convincing LensLib covering possible aberration behaviors of real-world lenses is first constructed to pre-train a base model with strong generalization capabilities. To achieve this, instead of manual design or collection, we propose a novel Evolution-based Automatic Optical Design (EAOD) method for automatic LensLib generation, consisting of an evolution mechanism for enriching the diversity of the generated lens structures, and comprehensive optimization objectives to ensure their reasonable aberration behaviors. As shown in Fig. 1 (c), the model pre-trained on automatically generated LensLib generalizes well to the training-unseen lenses. Then, incorporating the easily accessible real-captured images of a specific lens, the LensLib-to-specific domain adaptation is conducted to fine-tune the pre-trained model for better specific CAC results. To this intent, we develop an efficient DA framework based on our statistic observation of Dark Channel Prior (DCP) [37] in optical degradation, which is expressed as an unsupervised regularization term to constrain the CAC model for fast and few-shot domain adaptation. Despite in a blind deconvolution way without access to the lens descriptions, the adapted model can achieve excellent results

as shown in Fig. 1 (d).

Extensive experiments under various testing lenses and networks further demonstrate that: i) The LensLib constructed by EAOD delivers state-of-the-art performance in training a robust blind universal CAC model; ii) The LensLib-based pre-training further improves the non-blind lens-specific model; iii) The LensLib-to-specific domain adaptation brings significant improvements to the base model, especially in tough and real-world cases.

In summary, OmniLens offers a solution for users without an optical background to CAC of an unknown lens, which also provides a robust pre-training foundation for research on non-blind lens-specific CAC. The main contributions are summarized as follows:

- We deliver a novel insight into universal CAC, modeling it as LensLib-to-specific domain adaptation.
- We design the Evolution-based Automatic Optical Design (EAOD) method to build up a convincing LensLib, developing a pre-trained foundation with strong generalization ability.
- An efficient and unsupervised DA framework is proposed to adapt the pre-trained model to specific lenses.
- Extensive experiments across 6 testing lenses and 3 networks verify the effectiveness of OmniLens for correcting diverse lens aberrations blindly with unknown lens descriptions, where the pre-trained foundation can also facilitate non-blind lens-specific solutions.

2. Related Work

Computational Aberration Correction. Computational Aberration Correction (CAC) [17, 42] is proposed to enhance the images of low-end lenses with optical degradation. Benefiting from the blooming development of image restoration networks in low-level vision [2, 3, 34], learning-based CAC methods [4, 7, 39] have revealed more impressive results than model-based methods [12, 43, 57]. These methods can be regarded as an implicit modeling of end-to-end non-blind deconvolution, wherein the model learns the deconvolution for a specific lens using data generated from calibrated or simulated lens descriptions. Yet, limited to lens-specific solutions, these models can hardly accommodate new unseen lenses. Recently, universal CAC [14, 31] has been explored for addressing the optical degradation of any lens blindly, where the generalization ability of the model highly depends on the coverage of the LensLib used for training. Existing LensLib construction centered around manually collected lens samples [14, 31], *i.e.*, ZEBASELib, or random Zernike model [20, 23], *i.e.*, ZernikeLib. However, the former suffers from the limited number and coverage, and the latter overlooks the domain shift between generated virtual lenses and real-world ones. Moreover, their fine-tuning pipelines are often not applicable in lens-descriptions-unknown scenarios. Consequently, we pro-

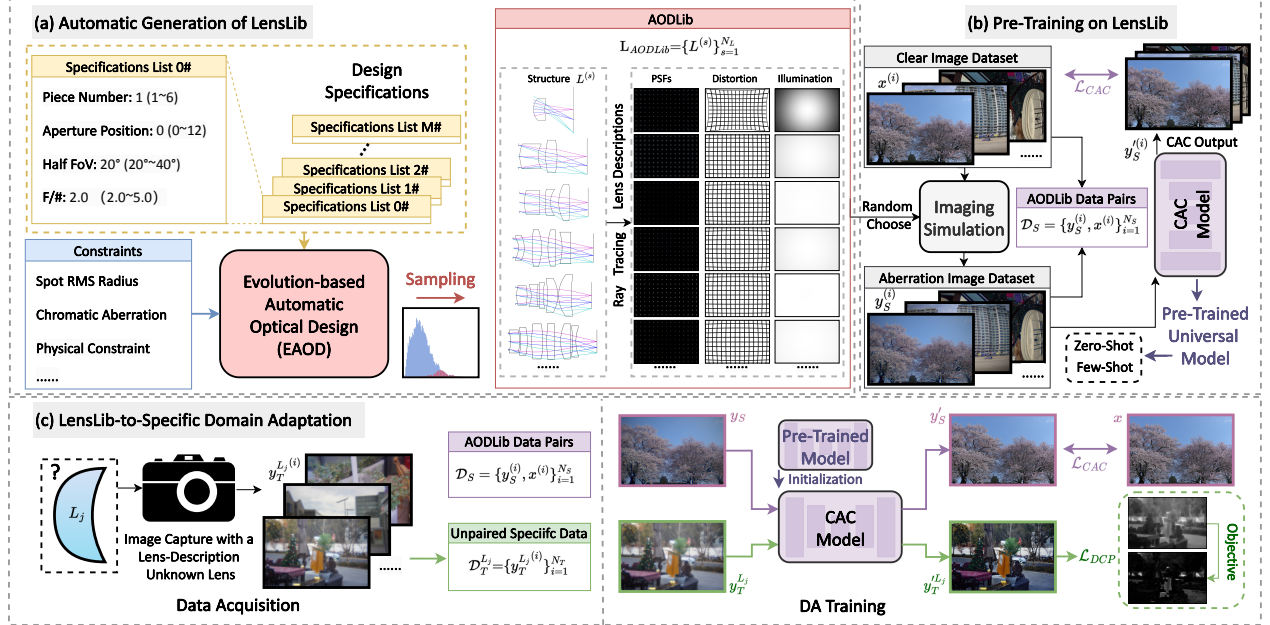


Figure 2. **Overview of the established OmniLens framework.** (a): The generation of AODLib by the proposed EAOD method with multiple design specifications and constraints fed in. (b) Based on the AODLib data pairs prepared by imaging simulation, we pre-train a universal CAC model for zero-shot or few-shot CAC of target lenses. (c): Incorporating the real-world captured images of the target lens-description unknown lens, LensLib-to-specific domain adaptation is conducted to fine-tune the pre-trained model for enhancing the results, where the DA training is guided by an unsupervised loss derived from DCP of the optical degradation.

pose OmniLens to address these limitations, constructing a more convincing LensLib by automatic optical design, and a LensLib-to-specific domain adaptation pipeline to fine-tune the model with unknown lens descriptions.

Automatic Optical Design. Heuristic algorithms, *e.g.*, Simulated Annealing (SA), Genetic Algorithm (GA), and Particle Swarm Optimization (PSO) have gained widespread adoption in the field of automatic optical design (AOD) [15, 40, 46, 49, 58, 60] for searching the optimized lens structure under the given constraints. Recently, Yang *et al.* have also proposed to combine curriculum learning and deep optics for achieving better AOD results [56]. However, existing works only focus on finding a certain optimal optical system, ignoring the exploration of possible diverse structures. Efforts have been made to pursue diverse design solutions using Deep Neural Networks (DNN) [10, 11]. Yet, their performance is restricted to the training lens database. Moreover, the lens structures output by the network are not regularized by any stringent quality or physical constraints, which can hardly cover the lenses in practical applications. To this end, we put forward the EAOD method based on heuristic algorithms to generate a diverse range of lenses automatically with machinable structures and reasonable aberration behaviors to cover real-world lenses.

Domain Adaptation in Low-Level Vision. Early effort has been made in mitigating the synthetic-to-real gap problem in CAC via domain adaptation from labeled synthetic domain to the unlabeled target real-world domain [24], which demands a large amount of data and training iterations for

learning the domain-mixing representation of optical degradation. Nevertheless, the optical degradation of LensLib varies across each training sample, which can hardly be represented in a uniform way mixed with the target-specific domain. The heavy training cost also renders such approaches unsuitable for the required rapid model fine-tuning in our framework. In addition, there have been works on domain adaptation in other low-level vision tasks, *e.g.*, image super-resolution [51, 54], image dehazing [8, 30, 32], and underwater image enhancement [21, 53]. Among them, we find that the utilization of task-specific physical priors (*e.g.*, DCP) [8, 30] contributed to effective adaptation with minimal training cost. To achieve this, we verify the existence of DCP in optical degradation, deriving it into a regularization term to enable the LensLib-to-specific domain adaptation.

3. Methodology

3.1. Framework Overview

A flexible two-stage framework OmniLens is introduced for universal CAC in real-world applications with unknown lens descriptions. As shown in Fig. 2 (a)~(b), the first stage is the *pre-training of a universal model on simulated data pairs under a LensLib*, where the core part is to generate possibly diverse and realistic lens samples by the EAOD method for constructing a convincing LensLib. To deal with the possible failure cases of the pre-trained model in a zero-shot manner confronted with unseen lenses, we propose a novel *LensLib-to-specific domain adaptation* pipeline for

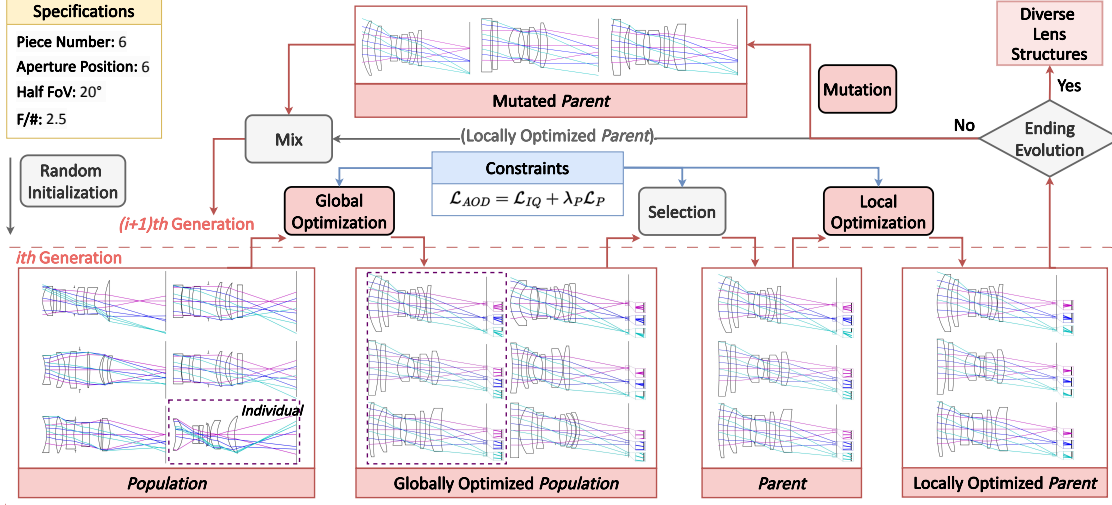


Figure 3. **Overall pipeline of the proposed EAOD method.** Taking the lens specifications of 6 piece as an example, the EAOD leverages a hybrid global and local optimization strategy to seek diverse lens structures that maximally satisfy both imaging quality and physical constraints from generation to generation based on an evolution framework with mutation mechanism.

the CAC of the target-specific lens at the second stage. As shown in Fig. 2 (c), the additional data required is solely a small number of real-world captured images by the target lens, which is easily accessible and requires no lens descriptions. The DA training is conducted based on the AODLib data pairs and the unpaired specific data, which is guided by both the unsupervised regularization derived from the observed DCP in optical degradation and the supervised loss.

3.2. Automatic Generation of LensLib

Considering the highly free and empirical process of optical design, designing a large number of lenses manually to traverse possible aberrations of real-world lenses is challenging. To tackle this issue, the idea of AOD [11] is introduced to enable the large-scale generation of lens samples.

Modeling the Automatic Optical Design. Overall, AOD aims to seek optimized lens structures under one given specifications set $\mathcal{S}^{(j)}$. To broaden the coverage of the designed lenses, four types of specifications that deliver large impacts on the final aberration behavior, *i.e.*, the piece number S_p , aperture position S_{aper} , half FoV S_{FoV} and F number S_F of the lens, are considered for composing $\mathcal{S}^{(j)}$. Then, we characterize a lens structure by its curvatures, surface parameters, glass and air spacings, refractive indexes, and Abbe numbers, defining a normalized lens parameters vector, whose dimension and value range meet the given specifications $\mathcal{S}^{(j)} = \{S_p^{(j)}, S_{aper}^{(j)}, S_{FoV}^{(j)}, S_F^{(j)}\}$:

$$P^{S^{(j)}} = (p^{(1)}, p^{(2)}, \dots, p^{(n)})^T \in \mathbb{R}^n. \quad (1)$$

The optimization process of $P^{S^{(j)}}$ is guided by an objective function $\mathcal{L}_{AOD}(P^{S^{(j)}})$, consisting of both imaging quality constraints and physical structure constraints. Specifically, an imaging quality loss \mathcal{L}_{IQ} calculated by ray-tracing [5]

is applied as the main optimization objective, which can be common RMS radius or Modulation Transfer Function (MTF) loss in traditional optical design[45]. Moreover, key physical properties of the lens derived from $P^{S^{(j)}}$ are constrained by a linear penalty to fall within a reasonable range:

$$\mathcal{L}_P = \frac{1}{n_P} \sum_{i=1}^{n_P} \alpha_i [\max(q_{min}^{(i)} - q_i, 0) + \max(q_i - q_{max}^{(i)}, 0)], \quad (2)$$

where n_P numbers of physical quantities q_i are constrained between $q_{min}^{(i)}$ and $q_{max}^{(i)}$, and the constraint ratio is regulated by weight α_i . We employ \mathcal{L}_P to ensure machinable output structures while meeting the specifications, in particular preventing adjacent surfaces from being too close together or even overlapped, which is a common error in the optical design process. Finally, \mathcal{L}_{AOD} considering both constraints with a balancing weight λ_P is expressed as:

$$\mathcal{L}_{AOD} = \mathcal{L}_{IQ} + \lambda_P \mathcal{L}_P. \quad (3)$$

Please refer to the supplemental document for more details about the implementation of \mathcal{L}_{AOD} . Finally, the AOD process can be modeled as:

$$\hat{P}^{S^{(j)}} = \arg \min \mathcal{L}_{AOD}(P^{S^{(j)}}), \quad (4)$$

where $\hat{P}^{S^{(j)}}$ is the optimized lens structure.

Evolution-based Automatic Optical Design. Based on the Eq. (4), we propose an EAOD method to (i) generate more possible lens structures under one set of specifications, and (ii) ensure the best imaging quality for the current structure for driving the aberration behaviors of the generated samples more close to those of real-world ones.

As shown in Fig. 3, EAOD builds upon a Genetic Algorithm (GA) [26] based evolution framework to pro-

duce optimized lens structures from generation to generation. We first define a *Population* composed of all lens structures to be optimized, where each structure is coined an *Individual*. Without any empirical preference, the *Individual* is the normalized lens parameters vector $P^{S^{(j)}}$ from random initialization, and m *Individuals* are initialized to constitute the *Population* for enriching diversity:

$$P^{S^{(j)}} = \{P_1^{S^{(j)}}, P_2^{S^{(j)}}, \dots, P_m^{S^{(j)}}\}. \quad (5)$$

Then, a hybrid global and local optimization strategy is proposed to find multiple promising high-quality structures $\hat{P}^{S^{(j)}}$ for $P^{S^{(j)}}$, coined the *Parent*, which minimizes the \mathcal{L}_{AOD} . Concretely, the global optimization method, *e.g.*, SA [41] or PSO [9], is employed to rapidly drive the randomly initialized *Individuals* towards the location of the global optimal solution, where the solutions with superior \mathcal{L}_{AOD} are selected for the following local optimization; while the local optimization method, *e.g.*, ADAM [28] or Damped Least Squares (DLS) [29], aims to seek their local optima for the relatively best imaging results under the primarily optimized structures. In addition, *Parent* is mutated for more possible structures, where for each *Individual* $\hat{P}_i^{S^{(j)}}$ in *Parent*, γ percentage of its parameters are randomly initialized. The mutated *Parent* is then mixed with the origin *Parent* to serve as the start points of the next generation. Finally, the hybrid optimization, selection, and mutation processes are re-conducted for each generation, where the *Parent* is outputted as the diverse lens structures when the generation meets the set number.

AODLib Construction. With all sets of specifications $S = \{S^{(j)}\}_{j=1}^M$ fed into EAOD, the initial LensLib L_{lib} is constructed. We further quantize its aberration behavior by using the average RMS spot radii (μm) of a lens sample (*RMS* for short), which can intuitively reflect the severity of the samples' aberrations. To mitigate the data preference towards any certain level of aberration, we propose to sample a portion of lenses from the L_{lib} to construct the final AODLib L_{AODLib} :

$$L_{AODLib} = \{L^{(s)}\}_{s=1}^{N_S} = \text{Sampling}(L_{lib}, r_{min}, r_{max}, N_S), \quad (6)$$

where we hope to obtain N_S samples with a uniform distribution of the *RMS* within the range $[r_{min}, r_{max}]$.

3.3. Pre-Training on LensLib

We employ a ray-tracing model [5] to calculate the lens descriptions for all samples in L_{AODLib} , which are applied to simulate aberration images via patch-wise convolution with clear images and distortion transformation. In this way, the AODLib data pairs $\mathcal{D}_S = \{y_S^{(i)}, x^{(i)}\}_{i=1}^N$ are prepared for supervised pre-training using the objective $\mathcal{L}_{CAC}(y_S^{(i)}, x^{(i)})$, where $y_S^{(i)}$ is the CAC output. \mathcal{L}_{CAC}

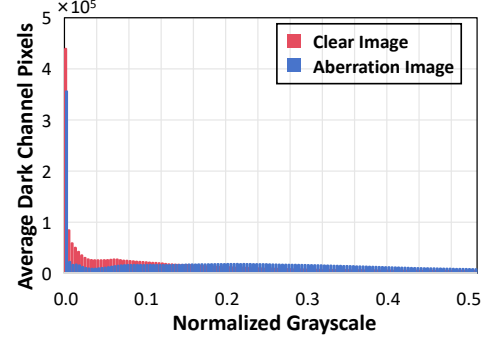


Figure 4. **Illustration of dark channel prior in CAC.** (a): The grayscale histogram of the DC images for aberration-clear image pairs. (b): The corresponding visual samples.

can be any training loss in the CAC field, such as the combination of L2 loss and perceptual loss [4], depending on the applied CAC model. The pre-trained universal model can be applied to correct aberrations of real-world lenses in a zero-shot manner. In addition, when the target lens description is available, it can serve as the pre-trained foundation for improving the lens-specific CAC model during few-shot fine-tuning or full model training.

3.4. LensLib-to-Specific Domain Adaptation

In this stage, few aberration images $\mathcal{D}_T^{L_j} = \{y_T^{L_j(i)}\}_{i=1}^{N_T}$ captured by the target lens L_j are utilized to adapt the pre-trained model trained on \mathcal{D}_S (the source domain) to $\mathcal{D}_T^{L_j}$'s optical degradation domain (the target domain).

Effective low-level vision DA frameworks [8, 21, 44] are often built upon the statistical priors of degraded images or clean images, *e.g.*, the Dark Channel Prior (DCP) [16] in image dehazing, which can provide an unsupervised regularization for model training. Motivated by the observation from [37] that convolution-induced blur often exhibits DCP, we hypothesize that optical degradation also adheres to DCP, as it originates from the convolution with the PSFs. To validate the hypothesis, we use the DIV2K dataset [50] of natural images, and without loss of generality, choose the second lens in Fig. 1 to construct aberration-clear image pairs. The Dark Channel (DC) image $D(I)$ for an image I can be calculated via a minimum value filtering operation:

$$D(I) = \min_{y \in \mathcal{N}(x)} (\min_{c \in \{r, g, b\}} I^c(y)), \quad (7)$$

Table 1. **Quantitative comparison with different LensLibs.** For conciseness, we only list the average performance of all test lenses. The detailed results can be found in the supplemental document. We highlight the **best** and **second best** results.

LensLib	Network	Params	Average Performance				
			PSNR \uparrow	SSIM \uparrow	LPIPS \downarrow	FID \downarrow	OS \uparrow
ZEBASELib [14, 31]	FOV-KPN	4.01M	24.01	0.748	0.2547	41.22	63.13
	SwinIR	11.97M	23.54	0.755	0.2618	41.07	62.82
	FeMaSR	37.37M	23.55	0.737	0.2288	38.76	64.28
ZernikeLib [20, 23]	FOV-KPN	4.01M	25.16	0.776	0.1910	33.56	68.76
	SwinIR	11.97M	24.45	0.784	0.1788	29.20	69.98
	FeMaSR	37.37M	23.73	0.758	0.1620	30.98	69.49
AODLib -LensNet [11]	FOV-KPN	4.01M	23.84	0.750	0.2466	41.09	63.54
	SwinIR	11.97M	24.79	0.773	0.2271	36.94	66.21
	FeMaSR	37.37M	23.79	0.748	0.2097	36.41	66.01
AODLib -EAOD (Ours)	FOV-KPN	4.01M	<u>25.62</u>	0.785	0.1902	27.16	70.21
	SwinIR	11.97M	26.13	0.817	<u>0.1622</u>	20.82	73.73
	FeMaSR	37.37M	25.13	<u>0.788</u>	0.1409	<u>22.88</u>	<u>73.22</u>

where I^c is the c th color channel, x, y are pixel locations, and $\mathcal{N}(x)$ represents an image patch centered at x . We statistically analyze the intensity distribution histograms of the $D(I)$ for all the aforementioned aberration-clear image pairs as shown in Fig. 4, where a set of visual samples of I and $D(I)$ is also provided. Corroborating our hypothesis, the elements in DC images for clear natural images mostly tend towards zero, while aberration images exhibit far more non-zero pixels in their DC images, indicating that optical degradation indeed possesses DCP.

Based on the observation, we derive the DCP into \mathcal{L}_{DCP} as an unsupervised constraint on the CAC output $y_T^{L_j^{(i)}}$ of the target lens L_j :

$$\mathcal{L}_{DCP} = \|D(y_T^{L_j^{(i)}})\|_1, \quad (8)$$

where the $D(y_T^{L_j^{(i)}})$ will be pulled towards zero to align with the dark channel distribution of natural clear images. To improve the stability of the DA training, we also adopt \mathcal{L}_{CAC} to provide supervision on the source domain AODLib data \mathcal{D}_S , constructing the overall training objective \mathcal{L}_{DA} :

$$\mathcal{L}_{DA} = \lambda_S \mathcal{L}_{CAC} + \lambda_T \mathcal{L}_{DCP}, \quad (9)$$

where λ_S and λ_T are loss weights.

4. Experiments and Results

4.1. Implementation Details

Evaluation Protocol. We manually design 6 different specific lenses as the test samples, including 4 spherical lenses (S-1P-I, S-1P-II, S-2P, and S-3P) and 2 aspherical lenses (AS-1P and AS-3P) of different piece numbers. A synthetic

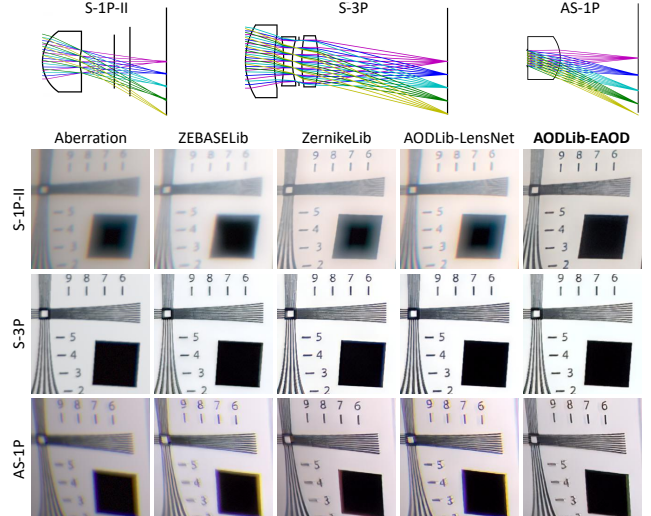


Figure 5. **Visual comparison with different LensLibs under 3 representative test lenses, which cover different surface types and levels of aberrations.** The optical paths of the 3 lenses are shown on the top of the figure. For each LensLib solution, we present its visual CAC results on an ISO12233 chart produced by FeMaSR which delivers the best perceptual performance.

benchmark of simulated images under each lens is then set up based on imaging simulation, where the referenced metrics, *i.e.*, PSNR, SSIM [52], LPIPS [61], and FID [19] are employed for comprehensive evaluation. We also normalize and weight these metrics following [35], constructing an Overall Score (OS) to intuitively evaluate the performance of each solution (detailed in supplement). In addition, we fabricate two of the single spherical lenses to capture test images for constructing a real-world benchmark.

Data Preparation. The Flickr2K [50] is chosen to generate \mathcal{D}_S . In terms of synthetic evaluation, to avoid information leakage, target-specific training data $\mathcal{D}_T^{L_j}$ and test data are prepared with another dataset DIV2K to simulate the real-world captured images, where the ground-truth is unavailable during DA training. For real-world evaluation, we capture 50 images as the test set, and another 25 images as $\mathcal{D}_T^{L_j}$, with each aforementioned fabricated lens.

AODLib Construction. Considering the optimization complexity, we only generate the spherical lens samples to ensure the quality of the optimized structures. In terms of EAOD, to balance optimization capability and convergence speed, we apply SAA and ADAM for the global optimization and local optimization respectively.

Model Training. We select FOV-KPN [4] (CNN and spatially-varying design), SwinIR [34] (Transformer), and FeMaSR [2] (CNN, Transformer, and generative model) as the representative networks in CAC to evaluate our OmniLens framework, all trained with default learning rates and loss functions for 200K iterations on \mathcal{D}_S to obtain the pre-training model. While for DA training, we use \mathcal{L}_{DA}

Table 2. **Quantitative evaluation of the OmniLens framework.** “*” denotes the additional data and iterations for training the lens-specific model. Similarly read as Tab. 1.

Solution	Network	Training Cost* (Imgs/Iters)	Average Performance				
			PSNR \uparrow	SSIM \uparrow	LPIPS \downarrow	FID \downarrow	OS \uparrow
<i>Lens-Descriptions-Unknown (Blind Deconvolution)</i>							
Eboli <i>et al.</i>	-	0/0K	22.07	0.689	0.3562	49.55	54.26
OmniLens Zero-Shot	FOV-KPN		25.62	0.785	0.1902	27.16	70.21
	SwinIR	0/0K	<u>26.13</u>	0.817	0.1622	<u>20.82</u>	73.73
	FeMaSR		25.13	0.788	0.1409	22.88	73.22
OmniLens DA	FOV-KPN		25.76	0.783	0.1845	24.84	70.84
	SwinIR	40/10K	26.18	<u>0.816</u>	0.1538	20.03	<u>74.26</u>
	FeMaSR		25.61	0.792	0.1260	20.03	74.70
<i>Lens-Descriptions-Known (Non-Blind Deconvolution)</i>							
<i>Few-Shot</i>							
Specific	FOV-KPN		23.97	0.764	0.2247	28.62	66.98
	SwinIR	105/10K	25.35	0.800	0.1911	22.04	71.28
	FeMaSR		24.11	0.768	0.1499	23.85	71.61
Specific +OmniLens	FOV-KPN		<u>26.05</u>	<u>0.804</u>	0.1613	18.95	73.63
	SwinIR	105/10K	26.86	0.836	<u>0.1386</u>	15.68	<u>76.54</u>
	FeMaSR		25.96	0.801	0.1077	<u>15.84</u>	76.65
<i>Full Training</i>							
Specific	FOV-KPN		26.42	0.810	0.1541	18.14	74.44
	SwinIR	2111/200K	<u>26.77</u>	<u>0.837</u>	0.1436	15.99	76.24
	FeMaSR		25.54	0.804	<u>0.1149</u>	17.00	76.04
Specific +OmniLens	FOV-KPN		26.61	0.817	0.1496	17.42	75.06
	SwinIR	2111/200K	27.09	0.841	0.1356	<u>15.18</u>	<u>77.01</u>
	FeMaSR		26.08	0.807	0.1010	14.59	77.40

with a window size of 15 for DC image calculation to fine-tune the pre-trained model for 10K iterations with a learning rate of $1e-6$, where λ_S and λ_T are set to 0.01 and 1 respectively, which is consistent across all 3 networks.

More details can be found in the supplemental document.

4.2. Comparison with Different LensLibs

As shown in Tab. 1, we first verify the effectiveness of AODLib built by EAOD via comparison with the other two LensLib pipelines, *i.e.*, the ZEBASELib and the ZernikeLib introduced in Sec. 2, whose construction process is consistent with [14] and [23] respectively. Additionally, the deep-learning-based AOD method LensNet [11] is also applied to construct a competing AODLib. The universal models with different architectures trained on our AODLib-EAOD outperform those under other LensLibs by a large margin, *e.g.*, achieving the best OS, and bringing average gains of $1.78dB \sim 1.93dB$ in PSNR and $-0.084 \sim -0.013$ in LPIPS. It can also be seen from the visual results in Fig. 5 that the CAC results of other pipelines still suffer from optical degradation under severe aberrations, where those of our method are sharp and clear. These evidences prove that the proposed EAOD method can build a more convincing LensLib for developing a robust universal CAC model generalizing well to most real-world lenses.

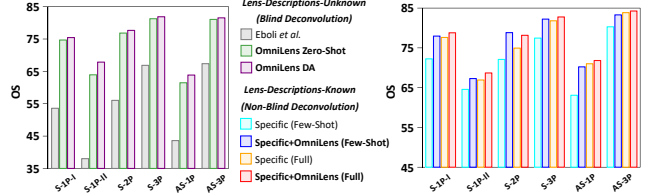


Figure 6. **Evaluation of OmniLens across all test lenses.** We show the OS results produced by FeMaSR with best performance.

4.3. Evaluation of OmniLens

In lens-descriptions-unknown cases, we compare our pre-trained model and DA model in OmniLens with the state-of-the-art blind deconvolution method Eboli *et al.* [12]. For cases with known lens descriptions, lens-specific models under the selected 3 networks are selected as baselines to evaluate OmniLens pre-training.

Synthetic Benchmark. Tab. 2 shows the average performance of competing methods in the synthetic benchmark, where Fig. 6 also provides detailed overall results across each test lens. In the lens-descriptions-unknown situation, the proposed OmniLens significantly outperforms traditional blind deconvolution method. Moreover, DA effectively improves the pre-trained model by $0.22dB$ in PSNR and -0.0096 in LPIPS. The improvements are observed across most test cases, which are more obvious under lenses with severe aberrations, *e.g.*, S-1P-I, S-1P-II, and AS-1P. Then, with known lens descriptions, OmniLens pre-training brings improvements to the lens-specific models under both few-shot ($1.81dB$ in PSNR and -0.0527 in LPIPS) and full training ($0.35dB$ in PSNR and -0.0088 in LPIPS) settings. Notably, even the few-shot specific model with OmniLens outperforms the full-trained one, illustrating OmniLens’s potential to serve as a CAC pre-training foundation.

Real-world Benchmark. Fig. 7 presents some of the results (top 4 solutions in Tab. 2) on real-world benchmark. Due to the synthetic-to-real domain gap, the results of lens-specific solution (3) reveal severe artifacts and unresolved optical degradation, while our OmniLens pre-training (1) and (4) can effectively suppress the artifacts. Moreover, OmniLens-DA (2) shows great advantages in this case, effectively handling the optical degradation (image blur and purple fringes) without introducing visually unpleasant artifacts. Benefiting from the regularization of \mathcal{L}_{CAC} on AODLib, the DA method can work in sky regions where DCP fails. The results of the user study are highly consistent with the visual results, where the results of OmniLens-based solutions are preferred by the majority of subjects.

4.4. Ablation Study

Without loss of generality, ablation studies are conducted with FeMaSR, presenting the average PSNR and LPIPS.

Ablations on Sampling Strategy. This ablation investi-

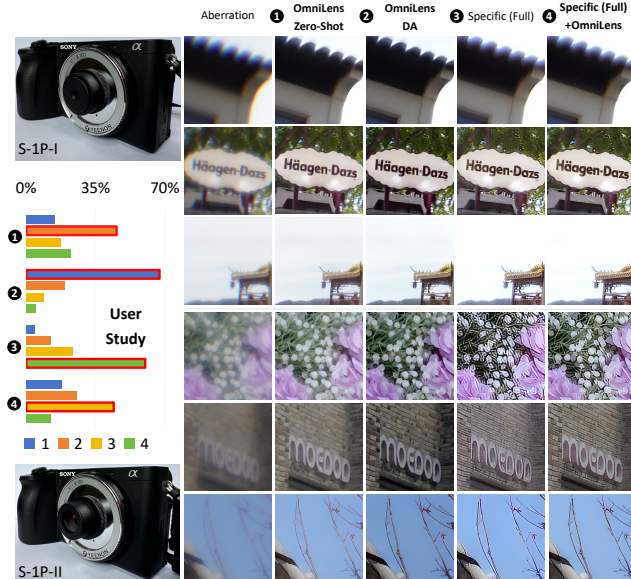


Figure 7. **Results on the real-world benchmark.** The shooting device for capturing real-world images is shown on the left of the figure, where the fabricated S-1P-I and S-1P-II are applied. We also present the results of a user study (detailed in the supplement), showing the percentage of each method ranked from first to fourth.

gates how to sample proper lenses to construct an effective AODLib. Tab. 3 shows the zero-shot results of the pre-trained model under AODLibs with different sampling settings to intuitively reflect the quality of sampled LensLibs. It can be observed that a uniform *RMS* distribution can eliminate the possible data preference, and more lens samples contribute to a larger coverage of LensLib.

Ablations on EAOD. We explore the effectiveness of the components in EAOD as shown in Tab. 4. Fixing S_p , experiments 1-4 illustrate the significance of the evolution mechanism, physical constraints, and global optimization for guaranteeing AODLib’s wide and realistic coverage to develop a robust universal model. Then, in terms of the implementation of the hybrid optimization strategy, we suggest the application of SA for global optimization and ADAM for local optimization to achieve better results (experiments 3, 5, 6). Moreover, experiments 3 and 7-10 reveal that each specification contributes to building a superior AODLib, where the absence of any one will limit the diversity of lens samples, resulting in a decline in model performance.

Ablations on DA Training. Tab. 5 reports the ablations on the usage of target images and DCP loss during DA training. From experiments 1-2, 4 and the zero-shot results, \mathcal{L}_{DCP} can improve the CAC results when employed only on \mathcal{D}_S , but incorporating target images with \mathcal{L}_{DCP} delivers superior results with improvements of $0.42dB$ in PSNR and -0.0077 in LPIPS. Furthermore, a few real-world captured target images (1%~5%) can enable effective DA training as shown in experiments 3-5, illustrating the flexibility of the OmniLens framework which can be easily implemented

Table 3. **Ablations on Sampling Strategy.** We mainly investigate the sampling distribution and number N_S here, where more ablations can be found in the supplemental.

	Distribution	N_S	PSNR \uparrow	LPIPS \downarrow
<i>w/o. Sampling</i>	<i>n.a.</i>	<i>n.a.</i>	25.61	0.1287
1	Gaussian	100	25.55	0.1385
2	uniform	100	25.59	0.1330
3	uniform	10	23.94	0.1592
4	uniform	1000	25.86	0.1214

Table 4. **Ablations on EAOD.** The zero-shot results of the pre-trained model under each setting are reported. Specification settings: $S_p=6$ for *w/o.* S_p , $S_{aper}=2$ for *w/o.* S_{aper} , $S_{FoV}=20^\circ$ for *w/o.* S_{FoV} , and $S_F=3.5$ for *w/o.* S_F . Phy. Con.: Physical Constraints. Whether to employ local optimization is not ablated as it is indispensable for optimizing reasonable lens structures.

	\mathcal{S}	Evolution	Phy. Con.	Global	Local	PSNR \uparrow	LPIPS \downarrow
1	<i>w/o. S_p</i>	✗	✓	SA	ADAM	21.45	0.2709
2	<i>w/o. S_p</i>	✓	✗	SA	ADAM	24.27	0.1742
3	<i>w/o. S_p</i>	✓	✓	SA	ADAM	25.50	0.1598
4	<i>w/o. S_p</i>	✓	✓	<i>w/o.</i>	ADAM	23.59	0.2015
5	<i>w/o. S_p</i>	✓	✓	PSO	ADAM	24.71	0.1675
6	<i>w/o. S_p</i>	✓	✓	SA	DLS	23.76	0.1655
7	<i>w/o. S_{aper}</i>	✓	✓	SA	ADAM	25.00	0.1307
8	<i>w/o. S_{FoV}</i>	✓	✓	SA	ADAM	25.42	0.1267
9	<i>w/o. S_F</i>	✓	✓	SA	ADAM	25.11	0.1682
10	<i>all</i>	✓	✓	SA	ADAM	25.86	0.1214

Table 5. **Ablations on DA Training.** “†” means that \mathcal{L}_{DCP} is used on \mathcal{D}_S . N_T : Number of applied target images in DA training.

	N_T	\mathcal{L}_{CAC}	\mathcal{L}_{DCP}	PSNR \uparrow	LPIPS \downarrow
zero-shot	0	✗	<i>w/o.</i>	25.13	0.1409
1	0	✓	<i>w/o.</i>	25.30	0.1350
2	0	✓	<i>w.s.</i> 15 \dagger	25.19	0.1337
3	5 (1%)	✓	<i>w.s.</i> 15	25.35	0.1262
4	40 (5%)	✓	<i>w.s.</i> 15	25.61	0.1260
5	800 (100%)	✓	<i>w.s.</i> 15	25.49	0.1253
6	40 (5%)	✓	<i>w.s.</i> 35	25.51	0.1257
7	40 (5%)	✓	<i>w.s.</i> 95	25.49	0.1264

in real-world cases. Additionally, experiments 4, 6, and 7 show that the window size (*w.s.*) for calculating \mathcal{L}_{DCP} reveals a minimal impact on the DA results, which is suggested to be set to 15 for ensuring computational efficiency.

5. Conclusion and Discussion

This paper introduces a flexible framework OmniLens for universal CAC based on pre-training on LensLib and LensLib-to-specific domain adaptation. A pre-training model with strong generalization ability is first developed based on a lens database AODLib. This is achieved by the proposed EAOD method for automatically designing large amount lens samples covering a diverse range of real-

world aberration behaviors. The pre-trained model also reveals the potential to serve as a powerful pre-trained foundation. Moreover, we develop an efficient domain adaptation method to deal with the specific lens with unknown lens descriptions based on the DCP property of optical degradation. For the first time, DA is verified to be an effective solution to universal CAC, improving the pre-trained model only with fast fine-tuning (about 1 hour) on a few easily accessible real-world captured images (25 images).

References

- [1] Tim Brooks, Ben Mildenhall, Tianfan Xue, Jiawen Chen, Dillon Sharlet, and Jonathan T. Barron. Unprocessing images for learned raw denoising. In *CVPR*, 2019. 12
- [2] Chaofeng Chen, Xinyu Shi, Yipeng Qin, Xiaoming Li, Xiaoguang Han, Tao Yang, and Shihui Guo. Real-world blind super-resolution via feature matching with implicit high-resolution priors. In *MM*, 2022. 2, 6, 15
- [3] Liangyu Chen, Xiaojie Chu, Xiangyu Zhang, and Jian Sun. Simple baselines for image restoration. In *ECCV*, 2022. 2
- [4] Shiqi Chen, Huajun Feng, Keming Gao, Zhihai Xu, and Yueting Chen. Extreme-quality computational imaging via degradation framework. In *ICCV*, 2021. 2, 5, 6, 15
- [5] Shiqi Chen, Huajun Feng, Dexin Pan, Zhihai Xu, Qi Li, and Yueting Chen. Optical aberrations correction in postprocessing using imaging simulation. *ACM Transactions on Graphics*, 2021. 1, 2, 4, 5, 13, 14, 15
- [6] Shiqi Chen, Ting Lin, Huajun Feng, Zhihai Xu, Qi Li, and Yueting Chen. Computational optics for mobile terminals in mass production. *IEEE Transactions on Pattern Analysis and Machine Intelligence*, 2023. 14
- [7] Shiqi Chen, Jingwen Zhou, Menghao Li, Yueting Chen, and Tingting Jiang. Mobile image restoration via prior quantization. *Pattern Recognition Letters*, 2023. 2
- [8] Zeyuan Chen, Yangchao Wang, Yang Yang, and Dong Liu. PSD: Principled synthetic-to-real dehazing guided by physical priors. In *CVPR*, 2021. 3, 5
- [9] Maurice Clerc and James Kennedy. The particle swarm - explosion, stability, and convergence in a multidimensional complex space. *IEEE Transactions on Evolutionary Computation*, 2002. 5
- [10] Geoffroi Côté, Jean-François Lalonde, and Simon Thibault. Extrapolating from lens design databases using deep learning. *Optics Express*, 2019. 3
- [11] Geoffroi Côté, Jean-François Lalonde, and Simon Thibault. Deep learning-enabled framework for automatic lens design starting point generation. *Optics Express*, 2021. 3, 4, 6, 7, 19
- [12] Thomas Eboli, Jean-Michel Morel, and Gabriele Facciolo. Fast two-step blind optical aberration correction. In *ECCV*, 2022. 2, 7
- [13] Shaohua Gao, Lei Sun, Qi Jiang, Hao Shi, Jia Wang, Kaiwei Wang, and Jian Bai. Compact and lightweight panoramic annular lens for computer vision tasks. *Optics Express*, 2022. 1
- [14] Jin Gong, Runzhao Yang, Weihang Zhang, Jinli Suo, and Qionghai Dai. A physics-informed low-rank deep neural network for blind and universal lens aberration correction. In *CVPR*, 2024. 2, 6, 7, 19
- [15] Dabo Guo, Liang Yin, and Guang Yuan. New automatic optical design method based on combination of particle swarm optimization and least squares. *Optics Express*, 2019. 3
- [16] Kaiming He, Jian Sun, and Xiaoou Tang. Single image haze removal using dark channel prior. *IEEE Transactions on Pattern Analysis and Machine Intelligence*, 2011. 5
- [17] Felix Heide, Mushfiqur Rouf, Matthias B. Hullin, Björn Labitzke, Wolfgang Heidrich, and Andreas Kolb. High-quality computational imaging through simple lenses. *ACM Transactions on Graphics*, 2013. 2
- [18] Felix Heide, Mushfiqur Rouf, Matthias B. Hullin, Björn Labitzke, Wolfgang Heidrich, and Andreas Kolb. High-quality computational imaging through simple lenses. *ACM Transactions on Graphics*, 2013. 1
- [19] Martin Heusel, Hubert Ramsauer, Thomas Unterthiner, Bernhard Nessler, and Sepp Hochreiter. GANs trained by a two time-scale update rule converge to a local nash equilibrium. In *NeurIPS*, 2017. 6
- [20] Lejia Hu, Shuwen Hu, Wei Gong, and Ke Si. Image enhancement for fluorescence microscopy based on deep learning with prior knowledge of aberration. *Optics Letters*, 2021. 2, 6, 19
- [21] Qun Jiang, Yunfeng Zhang, Fangxun Bao, Xiuyang Zhao, Caiming Zhang, and Peide Liu. Two-step domain adaptation for underwater image enhancement. *Pattern Recognition*, 2022. 3, 5
- [22] Qi Jiang, Shaohua Gao, Yao Gao, Kailun Yang, Zhonghua Yi, Hao Shi, Lei Sun, and Kaiwei Wang. Minimalist and high-quality panoramic imaging with PSF-aware transformers. *IEEE Transactions on Image Processing*, 2024. 15
- [23] Qi Jiang, Hao Shi, Shaohua Gao, Jiaming Zhang, Kailun Yang, Lei Sun, Huajian Ni, and Kaiwei Wang. Computational imaging for machine perception: Transferring semantic segmentation beyond aberrations. *IEEE Transactions on Computational Imaging*, 2024. 2, 6, 7, 19
- [24] Qi Jiang, Zhonghua Yi, Shaohua Gao, Yao Gao, Xiaolong Qian, Hao Shi, Lei Sun, JinXing Niu, Kaiwei Wang, Kailun Yang, and Jian Bai. Representing domain-mixing optical degradation for real-world computational aberration correction via vector quantization. *Optics & Laser Technology*, 2024. 3
- [25] Qi Jiang, Zhonghua Yi, Shaohua Gao, Yao Gao, Xiaolong Qian, Hao Shi, Lei Sun, JinXing Niu, Kaiwei Wang, Kailun Yang, et al. Representing domain-mixing optical degradation for real-world computational aberration correction via vector quantization. *Optics & Laser Technology*, 183:112080, 2025. 15
- [26] Sourabh Katoch, Sumit Singh Chauhan, and Vijay Kumar. A review on genetic algorithm: past, present, and future. *Multimedia Tools and Applications*, 2021. 4
- [27] Eric Kee, Sylvain Paris, Simon Chen, and Jue Wang. Modeling and removing spatially-varying optical blur. In *ICCP*, 2011. 1

- [28] Diederik P. Kingma and Jimmy Ba. Adam: A method for stochastic optimization. In *ICLR*, 2015. 5, 15
- [29] Kenneth Levenberg. A method for the solution of certain non-linear problems in least squares. *Quarterly of Applied Mathematics*, 1944. 5
- [30] Lerenhan Li, Yunlong Dong, Wenqi Ren, Jinshan Pan, Changxin Gao, Nong Sang, and Ming-Hsuan Yang. Semi-supervised image dehazing. *IEEE Transactions on Image Processing*, 2020. 3
- [31] Xiu Li, Jinli Suo, Weihang Zhang, Xin Yuan, and Qionghai Dai. Universal and flexible optical aberration correction using deep-prior based deconvolution. In *ICCV*, 2021. 1, 2, 6, 19
- [32] Xiaopeng Li, Hu Yu, Chen Zhao, Cien Fan, and Lian Zou. Dadrnet: Cross-domain image dehazing via domain adaptation and disentangled representation. *Neurocomputing*, 544: 126242, 2023. 3
- [33] Zongling Li, Qingyu Hou, Zhipeng Wang, Fanjiao Tan, Jin Liu, and Wei Zhang. End-to-end learned single lens design using fast differentiable ray tracing. *Optics Letters*, 2021. 12
- [34] Jingyun Liang, Jiezhong Cao, Guolei Sun, Kai Zhang, Luc Van Gool, and Radu Timofte. SwinIR: Image restoration using swin transformer. In *ICCVW*, 2021. 2, 6, 15
- [35] Jie Liang, Radu Timofte, Qiaosi Yi, Shuaizheng Liu, Lingchen Sun, Rongyuan Wu, Xindong Zhang, Hui Zeng, Lei Zhang, Yibin Huang, et al. NTIRE 2024 restore any image model (RAIM) in the wild challenge. In *CVPRW*, 2024. 6
- [36] Ting Lin, Shiqi Chen, Huajun Feng, Zhihai Xu, Qi Li, and Yueting Chen. Non-blind optical degradation correction via frequency self-adaptive and finetune tactics. *Optics Express*, 2022. 2
- [37] Jinshan Pan, Deqing Sun, Hanspeter Pfister, and Ming-Hsuan Yang. Blind image deblurring using dark channel prior. In *CVPR*, 2016. 2, 5
- [38] Adam Paszke, Sam Gross, Francisco Massa, Adam Lerer, James Bradbury, Gregory Chanan, Trevor Killeen, Zeming Lin, Natalia Gimelshein, Luca Antiga, Alban Desmaison, Andreas Köpf, Edward Z. Yang, Zachary DeVito, Martin Raison, Alykhan Tejani, Sasank Chilamkurthy, Benoit Steiner, Lu Fang, Junjie Bai, and Soumith Chintala. PyTorch: An imperative style, high-performance deep learning library. In *NeurIPS*, 2019. 15
- [39] Yifan Peng, Qilin Sun, Xiong Dun, Gordon Wetzstein, Wolfgang Heidrich, and Felix Heide. Learned large field-of-view imaging with thin-plate optics. *ACM Transactions on Graphics*, 2019. 2
- [40] Carsten Reichert, Tarik Gruhonjic, and Alois Herkommer. Development of an open source algorithm for optical system design, combining genetic and local optimization. *Optical Engineering*, 2020. 3
- [41] Rob A. Rutenbar. Simulated annealing algorithms: An overview. *IEEE Circuits and Devices Magazine*, 1989. 5
- [42] Christian J. Schuler, Michael Hirsch, Stefan Harmeling, and Bernhard Schölkopf. Non-stationary correction of optical aberrations. In *ICCV*, 2011. 1, 2
- [43] Christian J. Schuler, Michael Hirsch, Stefan Harmeling, and Bernhard Schölkopf. Blind correction of optical aberrations. In *ECCV*, 2012. 2
- [44] Yuanjie Shao, Lerenhan Li, Wenqi Ren, Changxin Gao, and Nong Sang. Domain adaptation for image dehazing. In *CVPR*, 2020. 5
- [45] Thomas Steinich and Vladan Blahnik. Optical design of camera optics for mobile phones. *Advanced Optical Technologies*, 1(1-2):51–58, 2012. 4
- [46] Jifeng Sun and Xiaotong Li. Automatic design of machine vision lens based on improved genetic algorithm and damped least squares. In *SPIE*, 2021. 3
- [47] Qilin Sun, Congli Wang, Qiang Fu, Xiong Dun, and Wolfgang Heidrich. End-to-end complex lens design with differentiate ray tracing. *ACM Transactions on Graphics*, 2021. 12
- [48] Jinli Suo, Weihang Zhang, Jin Gong, Xin Yuan, David J. Brady, and Qionghai Dai. Computational imaging and artificial intelligence: The next revolution of mobile vision. *Proceedings of the IEEE*, 2023. 1
- [49] Ziyao Tang, Matthias Sonntag, and Herbert Gross. Ant colony optimization in lens design. *Applied Optics*, 2019. 3
- [50] Radu Timofte, Eirikur Agustsson, Luc Van Gool, Ming-Hsuan Yang, Lei Zhang, Bee Lim, Sanghyun Son, Heewon Kim, Seungjun Nah, Kyoung Mu Lee, et al. NTIRE 2017 challenge on single image super-resolution: Methods and results. In *CVPRW*, 2017. 5, 6, 14
- [51] Wei Wang, Haochen Zhang, Zehuan Yuan, and Changhu Wang. Unsupervised real-world super-resolution: A domain adaptation perspective. In *ICCV*, 2021. 2, 3
- [52] Zhou Wang, Alan C. Bovik, Hamid R. Sheikh, and Eero P. Simoncelli. Image quality assessment: from error visibility to structural similarity. *IEEE Transactions on Image Processing*, 2004. 6
- [53] Zhengyong Wang, Liquan Shen, Mai Xu, Mei Yu, Kun Wang, and Yufei Lin. Domain adaptation for underwater image enhancement. *IEEE Transactions on Image Processing*, 2023. 2, 3
- [54] Yunxuan Wei, Shuhang Gu, Yawei Li, Radu Timofte, Longcun Jin, and Hengjie Song. Unsupervised real-world image super resolution via domain-distance aware training. In *CVPR*, 2021. 3
- [55] Xiaoqian Xu, Pengxu Wei, Weikai Chen, Yang Liu, Mingzhi Mao, Liang Lin, and Guanbin Li. Dual adversarial adaptation for cross-device real-world image super-resolution. In *CVPR*, 2022. 2
- [56] Xinge Yang, Qiang Fu, and Wolfgang Heidrich. Curriculum learning for ab initio deep learned refractive optics. *Nature Communications*, 2024. 3
- [57] Tao Yue, Jinli Suo, Jue Wang, Xun Cao, and Qionghai Dai. Blind optical aberration correction by exploring geometric and visual priors. In *CVPR*, 2015. 2
- [58] Wei Yue, Guang Jin, and Xiubin Yang. Adaptive particle swarm optimization for automatic design of common aperture optical system. *Photonics*, 2022. 3

- [59] Syed Waqas Zamir, Aditya Arora, Salman Khan, Munawar Hayat, Fahad Shahbaz Khan, and Ming-Hsuan Yang. Restormer: Efficient transformer for high-resolution image restoration. In *CVPR*, 2022. 2
- [60] Jiajun Zhang, Zhaofeng Cen, and Xiaotong Li. Automated design of machine vision lens based on the combination of particle swarm optimization and damped least squares. In *SPIE*, 2020. 3
- [61] Richard Zhang, Phillip Isola, Alexei A. Efros, Eli Shechtman, and Oliver Wang. The unreasonable effectiveness of deep features as a perceptual metric. In *CVPR*, 2018. 6
- [62] Yuanlong Zhang, Xiaofei Song, Jiachen Xie, Jing Hu, Jiawei Chen, Xiang Li, Haiyu Zhang, Qiqun Zhou, Lekang Yuan, Chui Kong, Yibing Shen, Jiamin Wu, Lu Fang, and Qionghai Dai. Large depth-of-field ultra-compact microscope by progressive optimization and deep learning. *Nature Communications*, 2023. 1

6. Loss Function for EAOD

6.1. Detailed Imaging Quality Constraints in EAOD

We quantify the average spot RMS radius across all sampled FoVs and wavelengths into \mathcal{L}_{spt} , and average lateral chromatic aberration into \mathcal{L}_c , whose weighted sum constitutes the imaging quality loss \mathcal{L}_{IQ} in Sec. 3.2 of the main text:

$$\mathcal{L}_{IQ} = \mathcal{L}_{spt} + \lambda_c \mathcal{L}_c. \quad (10)$$

Specifically, we quantify the average spot RMS radius across all sampled FoVs and wavelengths into \mathcal{L}_{spt} :

$$\mathcal{L}_{spt} = \frac{1}{n_f n_w} \sum_{i=1}^{n_f} \sum_{j=1}^{n_w} \sqrt{\frac{\sum_{k=1}^{n_r} [(x(i, j; k) - \overline{x(i, j)})^2 + y(i, j; k)^2]}{n_r}}. \quad (11)$$

Here, n_f represents the number of sampled FoVs, n_w represents the number of sampled wavelengths, n_r represents the number of sampled rays, $x(i, j; k)$ represents the image plane x coordinate of the k_{th} ray, traced at i_{th} sampled FoV and j_{th} sampled wavelength, $y(i, j; k)$ represents the image plane y coordinate of the k_{th} ray, traced at i_{th} sampled FoV and j_{th} sampled wavelength, and $\overline{x(i, j)}$ represents the x coordinate of the main ray at i_{th} sampled FoV and j_{th} sampled wavelength. We assume that the sampled object points are all in the x -axis direction so $\overline{y(i, j)}=0$.

Then, we quantify the average lateral chromatic aberration across all sampled FoVs into \mathcal{L}_c :

$$\mathcal{L}_c = \frac{1}{n_f} \sum_{i=1}^{n_f} (\max\{\overline{x(i, 1)}, \overline{x(i, 2)}, \dots, \overline{x(i, n_w)}\} - \min\{\overline{x(i, 1)}, \overline{x(i, 2)}, \dots, \overline{x(i, n_w)}\}). \quad (12)$$

Here, at each sampled FoV, \mathcal{L}_c quantifies the maximum distance between main ray positions across all sampled wavelengths.

Table 6. Physical constraints in EAOD.

Physical Property	Constraint Range
Curvature	$-0.1 \text{ mm}^{-1} \sim 0.1 \text{ mm}^{-1}$
Glass center thickness	$4 \text{ mm} \sim 15 \text{ mm}$
Air center spacing	$1 \text{ mm} \sim 15 \text{ mm}$
Refractive index	$1.51 \sim 1.76$
Abbe number	$27.5 \sim 71.3$
Effective Focal Length	$(\frac{14.3}{\tan(S_{FoV})} - 5 \text{ mm} \sim (\frac{14.3}{\tan(S_{FoV})} + 5) \text{ mm}$
Distortion	$-10\% \sim 10\%$
Edge Spacing	$1 \text{ mm} \sim 15 \text{ mm}$
Glass Edge Thickness	$5 \text{ mm} \sim 15 \text{ mm}$
Back Focal Length	$> 15 \text{ mm}$
Total Track Length	$< (S_p \times 25 + 15) \text{ mm}$
Image Height	$14.2 \text{ mm} \sim 14.4 \text{ mm}$

Notably, our \mathcal{L}_{spt} and \mathcal{L}_c require the support of a ray tracing model to facilitate the necessary optical calculations, which constructs the lens structure and traces the distribution of each object point on the image plane, enabling the computation of relevant spot and chromatic aberrations. We will provide a detailed description of the ray-tracing model in Sec. 7.

6.2. Detailed Physical Constraints in EAOD

In addition to the basic normalized lens parameters $PS^{(j)}$ (i.e., curvature, glass center thickness, air center spacing, refractive index, and abbe number) that we straightforwardly constrain the normalized values within the range $[0, 1]$, other key physical properties of the lens, derived from $PS^{(j)}$, are constrained by a linear penalty function to fall within a reasonable range, which is quantified into \mathcal{L}_P . Physical properties constrained by \mathcal{L}_P include effective focal length, distortion, edge spacing, glass edge thickness, back focal length, total track length, and image height. The above physical constraints are outlined in Table 6, in which S_{FoV} represents half FoV and S_p represents piece number.

7. Imaging Simulation Model

7.1. Overall Pipeline

In our imaging simulation pipeline, the aberration-induced optical degradation is characterized by the energy dispersion of the point spread function $PSF(x', y')$, where (x', y') represents image plane coordinates. Specifically, our simulation model applies the patch-wise convolution between the scene image I_S and $PSF(x', y')$ for generating the aberration image I_A :

$$I_A(x', y') \approx PSF(x', y') * I_s(x', y'). \quad (13)$$

Besides, an optional Image Signal Processing (ISP) pipeline is introduced to help construct more realistic aberration images [1]. In this case, the scene image I_S is replaced by the scene raw image I'_S , and the aberration image I_A is replaced by the aberration raw image I'_A . Specifically, we first sequentially apply the inverted Gamma Correction (GC), inverted Color Correction Matrix (CCM), and inverted White Balance (WB) to I_S to obtain the scene raw image I'_S . The inverted ISP pipeline can be formulated as

$$I'_S = P_{WB}^{-1} \circ P_{CCM}^{-1} \circ P_{GC}^{-1}(I_S), \quad (14)$$

where \circ is the composition operator. P_{WB} , P_{CCM} , and P_{GC} represent the procedures of WB, CCM, and GC, respectively. After conducting patch-wise convolution with the $PSF(x', y')$, we mosaic the degraded raw image I'_A before adding shot and read noise to each channel. Moreover, we sequentially apply the demosaic algorithm, *i.e.*, WB, CCM, and GC, to the R-G-G-B noisy raw image, where the aberration-degraded image I_A in the sRGB domain is obtained. The ISP pipeline can be defined as:

$$I_A = P_{GC} \circ P_{CCM} \circ P_{WB} \circ P_{demosaic} \circ (P_{mosaic}(I'_A) + N), \quad (15)$$

where N represents the Gaussian shot and read noise. P_{mosaic} and $P_{demosaic}$ represent the procedures of mosaicking and demosaicking respectively.

7.2. Optical Ray-Tracing Model

To obtain accurate $PSF(x', y')$, we build a ray-tracing-based optical model. For the sake of convenience in presentation, all the symbol notations used here are independent of the representations in the main text. The reader can simply refer to the definitions provided here to clearly understand their meanings.

For a spherical optical lens, its structure is determined by the curvatures of the spherical interfaces c , glass and air spacings s , and the refractive index n and Abbe number v of the material. Specifically, n represents the refractive index at the “ d ” Fraunhofer line (587.6nm). Following [47], we use the approximate dispersion model $n(\lambda) \approx A + B/\lambda^2$ to retrieve the refractive index at any wavelength λ , where A and B follow the definition of the “ d ”-line refractive index and Abbe number. Thus, the lens parameters can be denoted as $\phi_{lens} = (c, s, n, v)$. Assuming that there is no vignetting, after the maximum field of view θ_{max} and the size of aperture stop r_{aper} are determined, the ray tracing is performed. The traditional spherical surface can be expressed as:

$$z = \frac{cr^2}{1 + \sqrt{1 - c^2r^2}}, \quad (16)$$

where r indicates the distance from (x, y) to the z-axis: $r^2 = x^2 + y^2$. Then, we conduct sampling on the entrance pupil. The obtained point $\mathbf{S} = (x, y, z)$ can be regarded

as a monochromatic light source and its propagation direction is determined by the normalized direction vector $\mathbf{D} = (X, Y, Z)$. The propagation process of light between two surfaces can be defined as:

$$\mathbf{S}' = \mathbf{S} + t\mathbf{D}, \quad (17)$$

where t denotes the distance traveled by the ray. Therefore, the process of ray tracing can be simplified as solving the intersection point \mathbf{S}' of the ray and the surface, together with the direction vector \mathbf{D}' after refraction. By building the simultaneous equations of Eq. 16 and Eq. 17, the solution t can be acquired. After substituting t into Eq. 17, the intersection point \mathbf{S}' can be obtained, while the refracted direction vector \mathbf{D}' can be computed by Snell’s law:

$$\mathbf{D}' = \frac{n_1}{n_2} \left[\mathbf{D} + \left(\cos\langle \mathbf{p}, \mathbf{D} \rangle - \sqrt{\frac{n_2^2}{n_1^2} - 1 + \cos^2\langle \mathbf{p}, \mathbf{D} \rangle} \right) \mathbf{p} \right], \quad (18)$$

where \mathbf{p} is the normal unit vector of the surface equation, n_1 and n_2 are the refractive indices on both sides of the surface, \mathbf{D} is the direction vector of the incident light, and $\cos\langle \cdot, \cdot \rangle$ is the operation for calculating cosine value between two vectors. By alternately calculating the intersection point \mathbf{S}' and the refracted direction vector \mathbf{D}' , rays can be traced to the image plane to obtain the PSFs. Under dominant geometrical aberrations, diffraction can be safely ignored and the PSFs can be computed through the Gaussianization of the intersection of the ray and image plane [33]. Specifically, when the ray intersects the image plane, we get its intensity distribution instead of an intersection point. The intensity distribution of the ray on the image plane can also be described by the Gaussian function:

$$E(m, n) = \frac{1}{\sqrt{2\pi}\sigma} \exp\left(-\frac{r(m, n)^2}{2\sigma^2}\right). \quad (19)$$

$r(m, n)$ is the distance between the pixel indexed as (m, n) and the center of the ray on the image plane, which is just the intersection point in conventional ray tracing, and $\sigma = \sqrt{\Delta x^2 + \Delta y^2}/3$. By superimposing each Gaussian spot, the final PSFs can be obtained.

To sum up, the PSFs of all FoVs can be formulated as:

$$PSF(x', y') = T(c, s, n, v, \theta_{max}, r_{aper}; x', y'), \quad (20)$$

where $T(\cdot)$ refers to the setup ray tracing model. Therefore, we can produce the synthetic aberration image by feeding the lens parameters $(c, s, n, v, \theta_{max}, r_{aper})$ to the imaging simulation pipeline.

7.3. Additional Details

During the imaging simulation process, to enhance the robustness of the synthetic data for addressing potential real-world scenarios, we also perform data augmentation for ISP

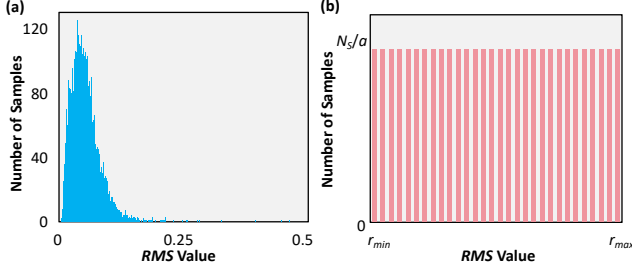


Figure 8. **Illustration of our sampling strategy.** (a): The RMS distribution of initial LensLib L_{lib} . (b): The ideal RMS distribution of the final AODLib L_{AODLib} .

and distortion. We first introduce ISP enhancement to obtain a new ground truth. Specifically, a set of ISP parameters is utilized to transform the image into the raw image via inverse ISP [5], which is converted into the enhanced image with the parameters perturbed by $\pm 5\%$ via ISP. Then, the optical degradation of the selected lens is applied to the new ground truth through patch-wise convolution and noise simulation, producing the aberration image. Last but not least, distortion transformation is conducted on both the aberration image and new ground truth, constructing the final aberration-clear data pair. In this way, the paired aberration images and ground truth images in synthetic data share the same ISP offsets and distortions. The model trained on such data will only remove the optical degradation while preserving the ISP offsets and distortions. We aim to leverage this enhancement to improve the robustness of the CAC model when dealing with the presence of ISP offsets and distortions, which are common in the real-world captured images of low-end lenses.

8. Sampling Strategy

8.1. More Details on Sampling Strategy

Without any explicit design in EAOD to deliver reasonable distribution for aberration behaviors of the generated lens samples, it is still difficult to train a general CAC model with strong generalization ability on the initial LensLib L_{lib} . We use the average RMS spot radii (mm) across all FoVs and wavelengths (RMS for short) of a lens to quantify its aberration behavior, which can intuitively reflect the severity of its aberrations, drawing the RMS distribution histogram, *i.e.*, the aberration distribution, of L_{lib} in Fig. 8 (a). It can be observed that the RMS of most samples in L_{lib} is concentrated in the middle range, which means that the samples of severe or mild aberrations are relatively scarce, unconsciously introducing data preference issues.

To overcome this issue, we propose a sampling strategy to sample a portion of lenses from the L_{lib} to construct the final AODLib L_{AODLib} with a relatively reasonable RMS

distribution under a given sampling number N_S :

$$L_{AODLib} = \{L^{(s)}\}_{s=1}^{N_S} = \text{Sampling}(L_{lib}, r_{min}, r_{max}, N_S). \quad (21)$$

Ideally, as shown in Fig. 8 (b), we hope to obtain a uniform distribution of the RMS within the range $[r_{min}, r_{max}]$ for the L_{AODLib} , mitigating the data preference towards any certain level of aberration, where $[r_{min}, r_{max}]$ determines L_{AODLib} 's coverage scope of aberration levels. Specifically, $[r_{min}, r_{max}]$ is divided into a sub-intervals, and N_S/a samples are randomly sampled from each of them, to achieve a relative uniform distribution across these sub-intervals. Yet, due to the powerful optimization capability of EAOD, only a few samples with exceptionally large RMS values are generated. When r_{max} and N_S are large, the number of samples in some sub-intervals is not enough for the required N_S/a . Consequently, we adjust the value of a via iteration, until the number of samples falling within each sub-interval reaches N_S/a .

8.2. Additional Ablations on Sampling Range and Distribution

In addition to the ablation studies on N_S and distribution presented in the main text, we provide the results of ablation studies on the sampling range and additional sampling distributions in Tab. 7, where the results in the main text are also presented. A wider RMS range contributes to a larger coverage of AODLib, improving the overall performance. However, considering that it is difficult to sample enough examples with an even wider range, the $[r_{min}, r_{max}]$ is set to $[0, 2.0]$ for the maximum coverage possible. Then, the uniform sampling strategy is crucial for training a robust CAC model, where other sampling distributions, even increasing the proportion of samples with severe aberrations (ascending), cannot yield better results. In terms of the choice of N_S , it appears evident that sampling more samples ensures the diversity of aberration behaviors in AODLib, contributing to superior generalization ability. Yet, the improvements are marginal when N_S is too large, where the uniform sampling becomes harder to achieve. Consequently, we set $N_S=1000$ as the final choice.

9. More Implementation Details

Evaluation Protocol. The optical paths of the 6 test lenses with their PSFs and RMS radius in 5 representative FoVs are shown in Fig. 9. We can observe that these 6 lenses, composed of varying numbers of spherical and aspherical optical elements, exhibit diverse aberration behaviors and severity levels. They encompass a range of samples, from small to large aberrations, spatially uniform to spatially variant distributions, and minimal to significant chromatic aberrations. In this way, the performance of the universal CAC model on these lenses adequately demonstrates its

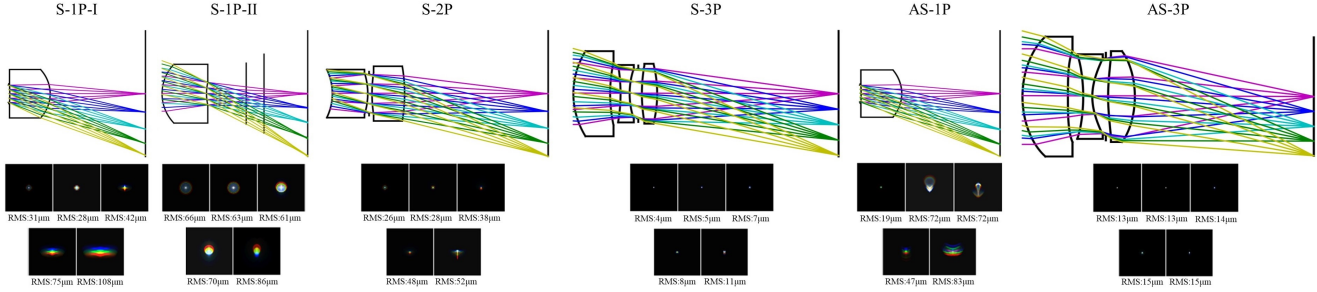


Figure 9. **The optical paths of the 6 test lenses with their PSFs and RMS radius in 5 representative FoVs.** PSFs are presented in the form of RGB maps, where the clearer the three colors of PSFs, the more severe the chromatic aberration. Best viewed on a screen and zoomed in.

Table 7. Additional ablations on sampling range and distribution. “ascending” and “degression” refer to the number of samples increasing or decreasing, respectively, as the *RMS* value increases.

	$[r_{min}, r_{max}]$	Distribution	N_S	PSNR	LPIPS
<i>w.o. Sampling</i>	<i>n.a.</i>	<i>n.a.</i>	<i>n.a.</i>	25.61	0.1287
1	[0, 0.05]	uniform	100	25.20	0.1639
2	[0, 0.1]	uniform	100	25.19	0.1421
3	[0, 0.2]	uniform	100	25.59	0.1330
4	[0, 0.2]	ascending	100	24.88	0.1412
5	[0, 0.2]	degression	100	25.63	0.1348
6	[0, 0.2]	Gaussian	100	25.55	0.1385
7	[0, 0.2]	uniform	10	23.94	0.1592
8	[0, 0.2]	uniform	1000	25.86	0.1214

generalization capability to various unseen lenses, ensuring the reliability of our evaluation protocol.

Imaging Sensor. The impact of optical degradation on images is further influenced by the pixel size of the sensor: for optical PSFs of the same physical dimensions (μm), smaller pixel size results in a greater number of pixels being affected, determining the specific pixel dimensions (pixels) of the PSFs. Our test lenses are mounted on a Sony $\alpha 6600$ camera, which features a sensor pixel size of approximately $3.9\mu m$, capturing images at a resolution of 6000×4000 . However, considering the current availability of training data predominantly in $2K$ resolution for clear images, we downsample all images in our experiments to 1920×1280 . In this context, for aberration images, the corresponding PSF pixel dimensions are downsampled at the same ratio, resulting in an equivalent pixel size of $12.19\mu m$. At the equivalent pixel size, PSFs with physical dimensions smaller than $12.19\mu m$ are sampled into a single pixel, thereby incapable of inducing optical degradation. Consequently, the lens with the smallest optical degradation in our test set (AS-3P) with a PSFs physical geometric radius

of $18\mu m$ (1.5 pixels), is equivalent to some high-end lenses (approximately $4\mu m$ of PSFs physical size, corresponding to a $3\mu m$ pixel size).

Data Preparation. We choose and reshape 2111 natural images with a resolution of 1920×1280 from the Flickr2K dataset [50] as the ground-truth to generate training dataset D_S based on the AODLib L_{AODLib} . For each image, a lens sample is randomly selected from L_{AODLib} , whose lens descriptions are fed into a comprehensive imaging simulation pipeline [5] with the image, considering the impacts of both the ISP and distortion. In this way, we prepare a convincing training set D_S for universal CAC. As a competing solution, we also prepare training data for the lens-specific method. For each target lens, a training set is constructed on the same ground-truth images as D_S to train a lens-specific model. Following the common practice [6], the perturbation method is employed to address the potential synthetic-to-real gap issue in lens-specific method, where 5 sets of perturbed lens parameters of the target lens within a $\pm 5\%$ range are randomly selected to be fed into the aforementioned simulation pipeline. In terms of the test set for evaluation, to avoid information leakage, the validation set of another natural images dataset DIV2K (92 images of 1920×1280) is utilized to generate the test image pairs for each target lens. Different from training data preparation, for test images, we conduct a once $\pm 2.5\%$ range of perturbation on the lens parameters to simulate the gap between the real lenses and the simulated ones. Similarly, the un-paired training data $D_T^{L_j}$ for DA training is prepared with 5% of DIV2K’s training set, where the ground truth is unavailable following the unsupervised training rule.

AODLib Construction. The value ranges for design specifications are consistent with those shown in Fig. 2 (a) of the main text, *i.e.*, 1~6 for piece number with an interval of 1, $20^\circ \sim 40^\circ$ for half FoV with an interval of 2° , and 2.0~5.0 for F number with an interval of 0.3. Notably, the aperture position is determined based on the piece number, which can be located before or after each piece for a given piece

number. In terms of the evolution strategy in EAOD, the degree of mutation is set to 30, and the number of generations is set to 20, to ensure the diversity of the generated lens structures. In addition, \mathcal{L}_P is used on effective focal length, distortion, edge spacing, glass edge thickness, back focal length, total track length, and image height, with α_i being $\{0.1, 1, 0.1, 0.1, 0.05, 0.01, 1\}$. The loss weights for \mathcal{L}_{AOD} are set as $\lambda_c=0.25$ and $\lambda_P=1$ empirically. Based on the above settings, we generate about 12,000 lens structures through EAOD, which are sampled by the sampling strategy. Specifically, the N_S , r_{min} , r_{max} , a are set to $\{1000, 0, 2.0, 2\}$ for sampling 1000 samples with a uniform *RMS* distribution over $[0, 2.0]$.

Chosen of CAC Networks. This work primarily focuses on deep learning-based CAC methods, which implicitly model deconvolution through end-to-end learning, enabling a network to directly learn this deconvolution mapping. Such methods can benefit from advancements in image restoration, demonstrating superior potential compared to traditional optimization-based algorithms [4, 5]. In this case, when the lens-descriptions are unknown (for our zero-shot and DA setting), the model learning universal deconvolution across multi-aberrations databases (*e.g.*, LensLib) can be considered as blind deconvolution. While for known lens-descriptions (calibrated or simulated PSFs), the model is trained on the data pairs of the specific lens generated based on the lens-descriptions, which is considered as non-blind deconvolution no matter whether the lens-descriptions are used in model inference, as it has learned the information of the specific lens. Additionally, our proposed OmniLens framework is centered on data construction and training strategies. In the main text, we selected 3 network architectures (FOV-KPN, SwinIR, and FeMaSR) renowned for their exceptional performance in the CAC field to validate the universality of OmniLens. These networks have been substantiated in related literature [4, 22, 25] as being well-suited for CAC tasks.

Model Training. In all the training processes in OmniLens, the Adam optimizer [28] is utilized with $\beta_1=0.9$, $\beta_2=0.99$ to train the model with a batch size of 8 on randomly cropped images of 256×256 . The model training is implemented with PyTorch [38] and on two NVIDIA GeForce RTX 3090 GPUs. The detailed training settings for each applied CAC network are provided in Table 8.

User Study. To conduct a subjective evaluation of the real-world results of OmniLens, we randomly sample five images from the real-world benchmark of the two fabricated lenses, respectively. 54 testers with normal visual ability were invited to participate in the experiment, where they needed to go through the imaging results of all the methods (the competitive non-blind specific baseline and 3 OmniLens solutions) in Fig. 7 of the main text and rank them based on image quality. The final results are presented as

Table 8. **Detailed training settings for applied CAC networks.** The combination of content, perceptual, and GAN loss constitutes \mathcal{L}_{CAC} for training the CAC model.

Network	LR	Scheduler	Content Loss	Perceptual Loss	GAN Loss
FOV-KPN [4]	1e-4	MultiStep	0.1 L2	1.0 LPIPS	w/o.
SwinIR [34]	2e-4	MultiStep	1.0 L1	1.0 LPIPS	w/o.
FeMaSR [2]	1e-4	MultiStep	1.0 L1	1.0 LPIPS	0.01 hinge

the percentage of each method ranked first, second, third, and fourth, as shown in Fig. 7 of the main text.

10. More Experimental Results

10.1. Detailed Results across All Test Lenses

Due to space constraints in the main text, we only present a partial set of test cases in experiments. Here, we provide the complete quantitative results across all test lenses for experiments of ‘‘Comparison with Different LensLibs’’ and ‘‘Evaluation of OmniLens’’ in the form of tables in Tab. 9~10. Given the substantial amount of data, we recommend zooming in for the best view.

From Tab. 9, the models trained on ZEBASELib, ZernikeLib struggle to handle cases with severe aberrations, *i.e.*, S-1P-I, S-1P-II, S-2P, and AS-1P-I, where AODLib-EAOD brings significant improvements over them. We believe that the impressive performance of AODLib-EAOD is due to its extensive coverage of aberration behaviors, which is lacking in ZEBASELib and ZernikeLib. For ZEBASELib, the trained model could overfit the database, as the number of manually collected samples is too small, which can hardly cover the possible aberration distributions in real-world lenses. Moreover, it is difficult to expand the size and coverage of such LensLibs, as commercial lens databases are often categorized by applications with sub-optimal structures, whose aberration behaviors are difficult to analyze and sort out manually. While the ZernikeLib seems a possible solution for batch-generation of virtual lens samples for a larger and broader LensLib, it overlooks the difference between the aberration distribution of the virtual lenses and real-world ones. The induced data domain gap also leads to failure cases in the CAC of unknown real-world lenses. In comparison, the coverage of our AODLib-EAOD is safeguarded by the GA-based evolution framework, while the aberration distribution is brought closer to the real-world one via the comprehensive optimization objectives and the hybrid global and local optimization strategy, making it a convincing database for universal CAC.

Then, we find that AODLib-LensNet delivers worse results than ZernikeLib in these severe aberration cases, indicating that not all AOD methods are capable of constructing a convincing LensLib. As shown in Fig. 11, the ab-

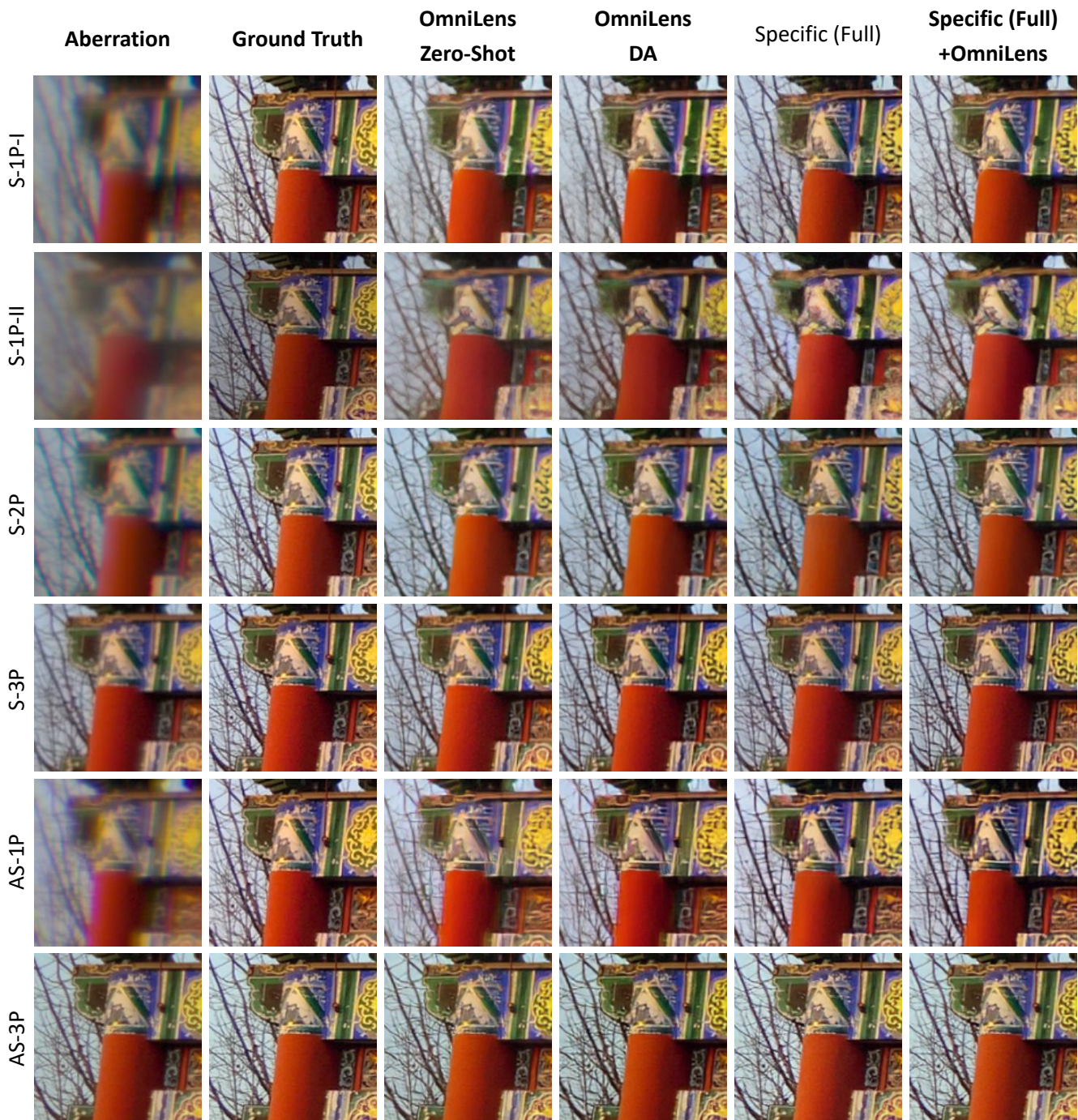


Figure 10. **Visual results across all test lenses on the synthetic benchmark.** These results are produced by FeMaSR, which reveals the best perceptual performance among the 3 applied networks. The pre-trained model in OmniLens demonstrates effective correction for the aberrations present in these test lenses, producing generally clear images. Additionally, the DA method can further enhance the CAC performance even in the absence of lens descriptions. With known lens descriptions, our pre-trained initialization can bring improvements of clearer details in the CAC results for lens-specific models, indicating that it can enhance the upper limit of lens-specific solutions.

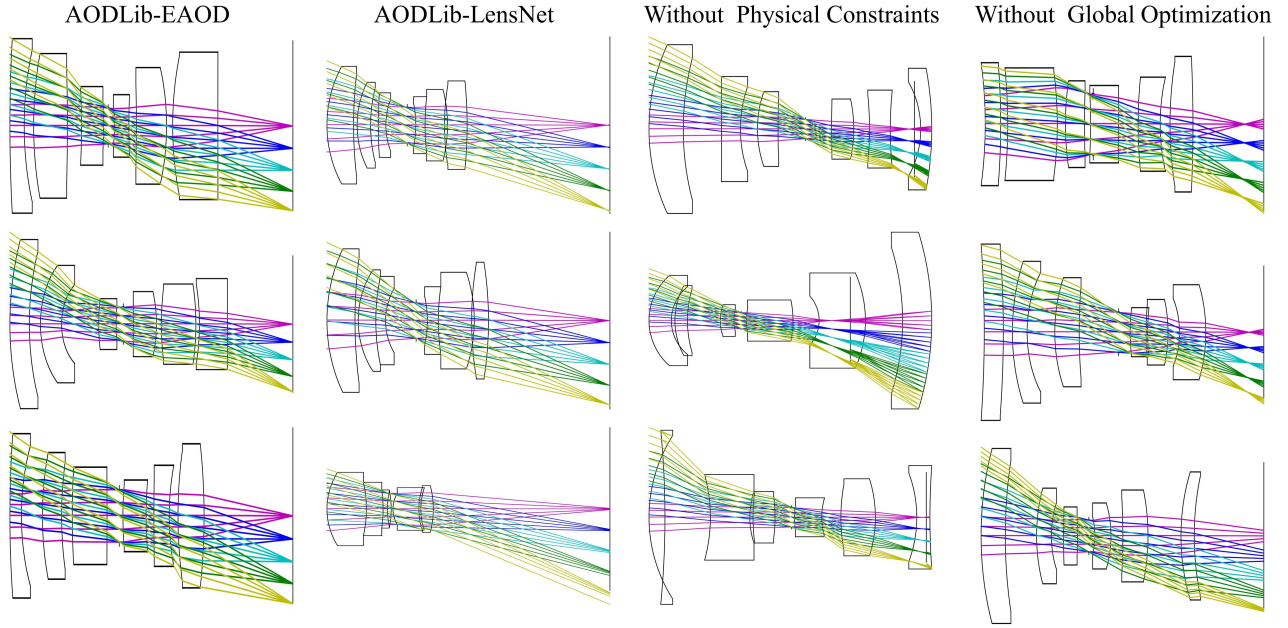


Figure 11. **Visualization of the generated lens structures under different AOD settings.** All the designs are under the same specifications set of $S_p = 6$, $S_{FOV} = 24^\circ$, $S_F = 4.4$, $S_{aper} = 6$.

sence of any stringent constraints during the output of lens structures by LensNet results in physical structural errors, such as overlapping adjacent surfaces, where the imaging quality has also not been optimized to the best for the current structure. Such lenses cannot serve as reliable samples within the LensLib for providing realistic aberration behaviors. Compared to LensNet, our EAOD method can generate lens samples with machinable structures with optimized imaging quality, which is a possible case in real-world applications. These evidences further illustrate that EAOD sets the state of the art in constructing a robust database for training a powerful universal CAC model.

Similar to that in the main text, the detailed evaluation results in Tab. 10 also demonstrate that OmniLens provides a robust and flexible solution to the universal CAC. We also provide corresponding visual results on the synthetic benchmark in Fig. 10 to further illustrate the effectiveness of OmniLens. It can be observed that the pre-trained model provided by OmniLens enhances the performance of the lens-specific model in all cases, while the DA method mainly improves the perceptual performance (LPIPS and FID), especially in cases with severe aberrations, where zero-shot models struggle to perform effectively. These pieces of evidence indicate that our proposed OmniLens is a comprehensive and flexible solution for universal CAC, allowing for the effective implementation of sub-schemes within OmniLens based on the severity of uncorrected aberrations and the availability of lens descriptions.

10.2. More Analysis of Tab. 4 in the Main Text

Tab. 11 presents the number of lens samples that can be automatically designed under different EAOD implementation schemes, providing a clear illustration of each EAOD component’s contribution to the generation of diverse lens structures.

From this, we can observe that the evolution mechanism is crucial for generating diverse lens structures, without which the number of generated lens structures is reduced by nearly 90%. This aligns with the significant decline in model performance observed in Tab. 4-experiment 1 of the main text.

Moreover, while removing physical constraints can increase the number of generated lens structures by relaxing selection criteria, it may result in overlapping surfaces (shown in Fig. 11), which is impossible in real-world lenses. Under this setting, the aberration behaviors of the EAOD-generated lenses deviate from those of real-world lenses, leading to the decline in model performance observed in experiment 2 of Tab. 4 in the main text.

In addition, the absence of global optimization in EAOD makes it challenging to produce high-quality optimized structures, resulting in many designs failing to meet the image quality screening criteria. This leads to a nearly 50% reduction in the final number of generated lens samples. Moreover, as shown in Fig. 11, the designed lens by such EAOD exhibits poor light focusing characteristics, failing to achieve optimal image quality under the current structure. Consequently, these designs are unlikely to occur in

real-world applications, contributing to a domain shift between the aberration behaviors of LensLib and real-world lenses. These findings explain the poor performance of the model observed in experiment 4 of Tab. 4 in the main text.

10.3. More Real-World Results

We present additional real-world results in Fig. 12 to show the generalization capability of our proposed OmniLens framework across diverse scenarios, encompassing indoor environments, outdoor architecture, outdoor vegetation, near and far views, pedestrians, and illuminated signage. Consistent with the results presented in the main text, lens-specific solutions tend to introduce severe artifacts due to the synthetic-to-real domain gap. To this end, incorporating the OmniLens pre-trained model can improve the CAC results, effectively alleviating the artifacts. Moreover, OmniLens successfully addresses the artifact problem in both zero-shot and DA settings without lens-descriptions, while the DA method further produces clearer details and removes most aberration-induced image blur which can hardly be achieved by the pre-trained model. It is noteworthy that the DA method results in an overall darker output due to the incorporation of the DCP constraint, which warrants further investigation in future work. However, as the DA training is simultaneously constrained by \mathcal{L}_{CAC} on the AODLib data, the limitations of DCP and its potential failure in certain scenarios (such as skies and indoor environments) do not yield visual-unpleasant CAC results, illustrating the robustness of OmniLens.

11. Discussion

11.1. Limitations and Future Work

In OmniLens, we develop a convincing training database AODLib-EAOD for universal CAC, which can also facilitate lens-specific solutions for providing a powerful pre-training foundation. Moreover, a LensLib-to-specific domain adaptation pipeline is proposed to deal with the failure cases of the pre-trained universal model, which can significantly improve the CAC performance on target-specific lenses only with unsupervised training on a few easily accessible real-captured images. However, some limitations require further exploration.

First and foremost, considering the complexity of optimization, the EAOD currently only accommodates spherical lens structures, leaving room for improvements in the coverage of AODLib. Introducing additional degrees of freedom in optimization, such as aspherical and diffractive elements, could yield design outcomes with richer aberration behaviors, which can hardly be achieved by spherical lenses. Therefore, enhancing the optimization capabilities of EAOD to achieve the automatic design of optical systems incorporating aspherical and diffractive elements represents

one of the important research directions for future work.

Additionally, the rich aberration behaviors of AODLib have not been fully leveraged during the training of our pre-trained model, as the model is merely fed with data from lenses with various aberrations in a random manner. We believe that appropriately classifying and annotating the aberration behaviors in AODLib, along with incorporating suitable prompts during model training, could enhance the generalization capability of the pre-trained models. In this context, we are particularly interested in utilizing prompt learning techniques in recent works of all-in-one image restoration.

11.2. Potential Negative Impacts

We explore a flexible universal CAC framework to address lens aberrations of arbitrary lenses, which is valuable for the applications of light-weight optical systems with uncorrected aberrations. This technology will facilitate the development of various mobile and wearable devices, such as mobile cameras, intelligent robots, and AR/VR equipment. However, the advantage of the tiny size of light-weight optical systems may also be leveraged for military reconnaissance and sneak shots. We hope that the relative applications can be regularized by laws to benefit our world.

Table 9. **Detailed quantitative comparison with other LensLibs.** We provide the results under all metrics (PSNR/SSIM/LPIPS/FID).

LensLib	Network	Spherical Lens				Aspherical Lens		
		1P-I	1P-II	2P	3P	1P	3P	3P
ZEBASELib [14, 31]	FOV-KPN	22.60/0.733/0.3051/40.26	22.15/0.649/0.4071/93.46	23.11/0.754/0.2711/33.57	28.51/0.859/0.1080/10.94	21.25/0.619/0.3510/57.52	26.42/0.873/0.0858/11.58	
	SwinIR	23.36/0.750/0.3036/39.68	17.68/0.618/0.4393/94.82	23.16/0.772/0.2705/32.14	27.66/0.871/0.1129/10.23	21.51/0.634/0.3622/59.24	27.87/0.883/0.0822/10.33	
	FeMaSR	23.98/0.749/0.2440/31.75	19.02/0.620/0.4055/83.09	23.82/0.757/0.2199/28.26	27.03/0.834/0.0932/15.26	21.73/0.628/0.3231/58.42	25.73/0.835/0.0871/15.76	
ZernikeLib [20, 23]	FOV-KPN	25.08/0.788/0.2135/26.85	21.82/0.704/0.2955/79.61	25.20/0.793/0.2061/24.89	29.29/0.856/0.0949/10.03	22.23/0.647/0.2639/47.97	27.34/0.869/0.0723/12.02	
	SwinIR	24.89/0.788/0.1953/23.27	18.82/0.701/0.2950/74.05	23.68/0.808/0.1833/21.27	28.85/0.872/0.0954/09.24	22.50/0.650/0.2339/37.32	27.96/0.885/0.0696/10.04	
	FeMaSR	23.58/0.761/0.1818/26.63	20.20/0.701/0.2558/69.46	23.99/0.786/0.1489/22.31	27.13/0.833/0.0879/13.07	21.52/0.624/0.2164/41.06	25.93/0.840/0.0809/13.35	
AODLib -LensNet [11]	FOV-KPN	22.19/0.736/0.2971/38.98	22.56/0.663/0.3606/93.20	22.52/0.740/0.2879/37.13	28.13/0.858/0.1213/11.06	21.29/0.624/0.3299/54.26	26.37/0.878/0.0830/11.92	
	SwinIR	24.57/0.783/0.2444/26.81	19.87/0.658/0.3823/89.61	23.97/0.764/0.2696/32.91	29.40/0.883/0.0962/08.75	22.39/0.654/0.3088/54.34	28.51/0.895/0.0615/09.24	
	FeMaSR	23.56/0.751/0.2353/29.02	21.18/0.656/0.3499/81.23	22.79/0.743/0.2581/32.22	27.51/0.851/0.0919/12.08	21.94/0.631/0.2534/49.98	25.73/0.855/0.0693/13.93	
AODLib -EAOD(Ours)	FOV-KPN	25.48/0.795/0.2085/24.79	23.39/0.715/0.2925/51.35	25.91/0.820/0.1819/17.81	29.54/0.861/0.1056/09.77	22.08/0.643/0.2789/47.69	27.32/0.878/0.0738/11.54	
	SwinIR	27.63/0.835/0.1631/16.43	20.17/0.747/0.2543/38.75	28.44/0.856/0.1570/13.53	29.49/0.887/0.0958/09.04	23.22/0.680/0.2374/37.10	27.82/0.895/0.0657/10.08	
	FeMaSR	26.39/0.803/0.1428/18.79	20.34/0.724/0.2059/37.49	26.87/0.823/0.1259/15.40	28.31/0.856/0.0822/10.82	22.48/0.659/0.2205/41.70	26.39/0.862/0.0680/13.08	

Table 10. **Detailed quantitative evaluation of OmniLens.** We provide the results under all metrics (PSNR/SSIM/LPIPS/FID).

Solution	Network	Spherical Lens				Aspherical Lens		
		1P-I	1P-II	2P	3P	1P	3P	3P
<i>Lens-Descriptions-Unknown (Blind Deconvolution)</i>								
Eboli <i>et al.</i>	-	20.58/0.687/0.3855/39.89	23.43/0.603/0.4918/99.00	20.84/0.697/0.3575/35.51	24.01/0.779/0.2362/28.71	20.47/0.571/0.4366/65.79	23.11/0.796/0.2296/28.37	
OmniLens Zero Shot	FOV-KPN	25.48/0.795/0.2085/24.79	23.39/0.715/0.2925/51.35	25.91/0.820/0.1819/17.81	29.54/0.861/0.1056/09.77	22.08/0.643/0.2789/47.69	27.32/0.878/0.0738/11.54	
	SwinIR	27.63/0.835/0.1631/16.43	20.17/0.747/0.2543/38.75	28.44/0.856/0.1570/13.53	29.49/0.887/0.0958/09.04	23.22/0.680/0.2374/37.10	27.82/0.895/0.0657/10.08	
	FeMaSR	26.39/0.803/0.1428/18.79	20.34/0.724/0.2059/37.49	26.87/0.823/0.1259/15.40	28.31/0.856/0.0822/10.82	22.48/0.659/0.2205/41.70	26.39/0.862/0.0680/13.08	
OmniLens DA	FOV-KPN	25.16/0.793/0.2051/24.57	25.35/0.724/0.2812/42.73	25.69/0.817/0.1800/17.23	29.30/0.858/0.1046/09.65	21.83/0.633/0.2627/43.57	27.21/0.875/0.0733/11.30	
	SwinIR	27.19/0.829/0.1597/16.23	21.92/0.763/0.2316/37.40	28.31/0.854/0.1543/12.87	29.22/0.883/0.0927/08.73	22.73/0.673/0.2200/35.10	27.72/0.895/0.0645/09.87	
	FeMaSR	26.50/0.802/0.1313/17.68	22.93/0.744/0.1778/31.64	26.97/0.825/0.1163/13.72	28.49/0.859/0.0763/09.80	22.63/0.656/0.1902/35.75	26.16/0.867/0.0640/11.56	
<i>Lens-Descriptions-Known (Non-Blind Deconvolution)</i>								
<i>Few-Shot</i>								
Specific	FOV-KPN	23.67/0.778/0.2474/28.42	21.92/0.695/0.3029/45.42	23.34/0.756/0.2552/27.72	27.10/0.842/0.1397/11.37	21.43/0.636/0.3134/46.69	26.33/0.877/0.0897/12.09	
	SwinIR	27.41/0.814/0.2096/20.03	20.24/0.732/0.2608/37.64	26.54/0.812/0.2064/18.88	27.34/0.853/0.1368/11.45	23.38/0.699/0.2641/33.22	27.16/0.892/0.0687/11.01	
	FeMaSR	25.47/0.779/0.1592/22.37	20.63/0.716/0.2010/34.17	24.94/0.781/0.1603/21.99	25.88/0.823/0.1036/16.04	21.70/0.649/0.2005/33.60	26.03/0.862/0.0747/14.94	
Specific+OmniLens	FOV-KPN	27.86/0.818/0.1767/16.61	20.47/0.728/0.2428/34.61	27.12/0.820/0.1683/16.29	29.13/0.861/0.0899/08.64	23.51/0.712/0.2192/27.00	28.21/0.885/0.0709/10.57	
	SwinIR	29.56/0.846/0.1468/12.79	19.98/0.768/0.2157/29.97	28.46/0.852/0.1385/12.40	28.65/0.882/0.0834/08.26	25.59/0.767/0.1899/22.48	28.90/0.902/0.0573/08.16	
	FeMaSR	27.91/0.811/0.1097/13.67	19.42/0.728/0.1677/26.24	27.59/0.821/0.0978/12.97	28.53/0.858/0.0703/09.41	24.26/0.708/0.1462/22.70	28.06/0.877/0.0546/10.07	
<i>Full Training</i>								
Specific	FOV-KPN	28.58/0.819/0.1642/15.05	19.63/0.732/0.2371/35.99	27.68/0.808/0.1793/17.51	29.72/0.861/0.0840/07.83	24.51/0.748/0.1943/22.87	28.37/0.890/0.0658/09.56	
	SwinIR	30.02/0.850/0.1338/12.34	19.92/0.771/0.2410/30.29	27.53/0.838/0.1567/15.46	28.02/0.885/0.0851/08.97	25.91/0.775/0.1931/20.79	29.24/0.905/0.0519/08.08	
	FeMaSR	27.10/0.812/0.1102/13.82	19.90/0.742/0.1813/28.21	25.39/0.797/0.1273/18.41	28.19/0.858/0.0755/09.56	24.25/0.731/0.1456/22.29	28.39/0.881/0.0495/09.72	
Specific+OmniLens	FOV-KPN	28.91/0.827/0.1564/14.29	19.51/0.747/0.2369/34.07	27.93/0.823/0.1670/15.60	29.94/0.859/0.0808/07.81	24.95/0.754/0.1894/22.57	28.44/0.889/0.0669/10.17	
	SwinIR	30.45/0.853/0.1320/11.49	19.89/0.773/0.2252/30.26	27.91/0.847/0.1430/13.81	28.18/0.885/0.0845/08.33	26.23/0.780/0.1710/19.45	29.85/0.906/0.0579/07.73	
	FeMaSR	27.96/0.811/0.0966/12.62	19.81/0.745/0.1590/24.21	26.73/0.813/0.0980/13.51	28.70/0.863/0.0667/08.43	24.70/0.729/0.1371/20.49	28.58/0.883/0.0483/08.28	

Table 11. **The number of lens samples generated under different EAOD implementation schemes.**

EAOD Components	Number of Lenses
<i>w.o.</i> S_{FoV}	3461
<i>w.o.</i> S_{aper}	3046
<i>w.o.</i> S_F	1179
<i>w.o.</i> S_p	1143
<i>w.o.</i> S_p & <i>w.o.</i> Evolution	128
<i>w.o.</i> S_p & <i>w.o.</i> Phy. Con.	2112
<i>w.o.</i> S_p & <i>w.o.</i> Global	565
<i>all</i>	12050

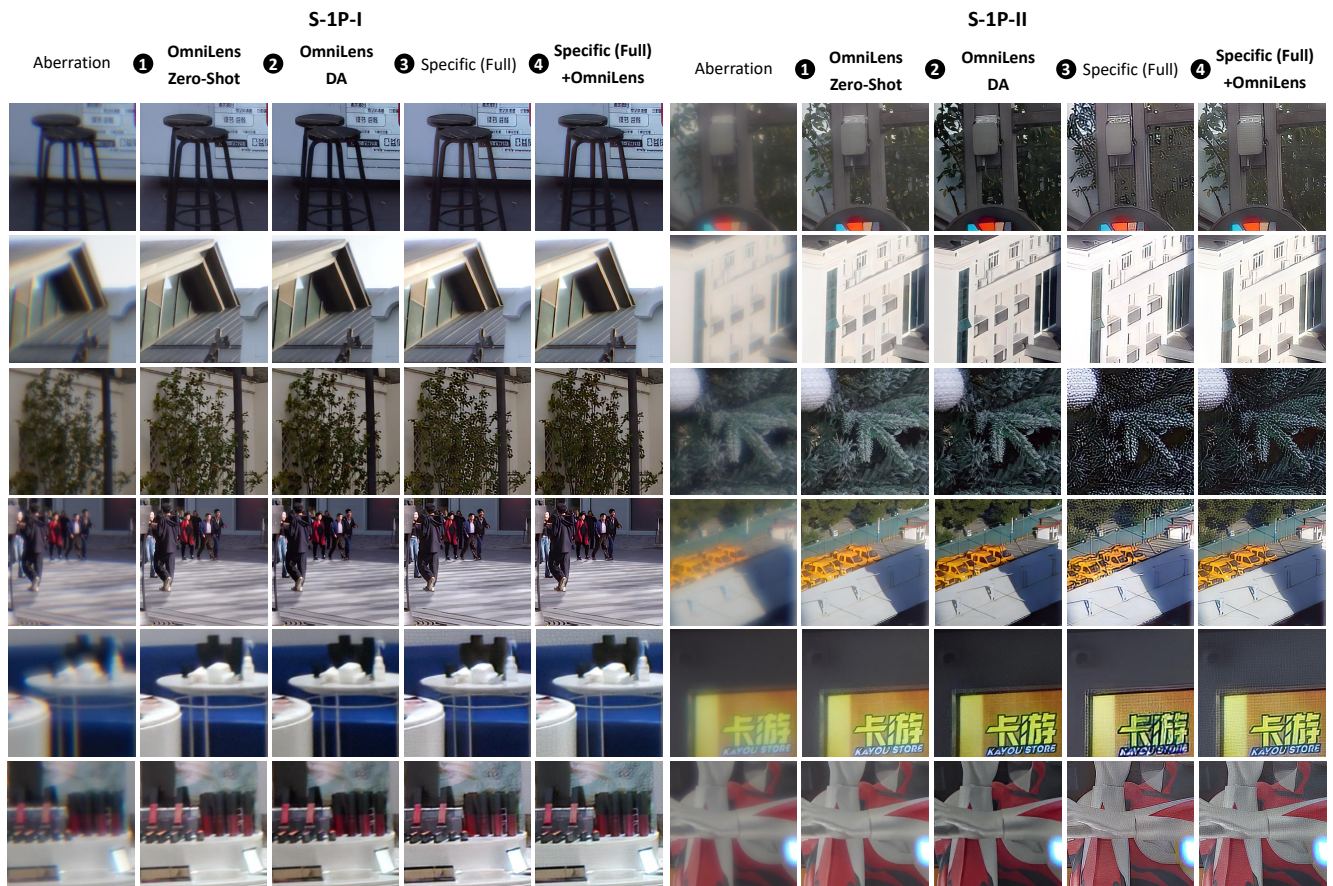


Figure 12. **Additional visual results on the real-world benchmark across diverse scenes.** Consistent with the results presented in the main text, when confronted with real-world images from lenses with severe aberrations, lens-specific solutions tend to introduce severe artifacts. However, incorporating the OmniLens pre-trained model effectively mitigates this issue. Moreover, OmniLens addresses the artifact problem in both zero-shot and DA settings without lens-descriptions, while the DA method further produces clearer details and removes most aberration-induced image blur.